

Average power density spectrum of *Swift* long gamma-ray bursts in the observer and in the source-rest frames

C. Guidorzi,^{1*} R. Margutti,² L. Amati,³ S. Campana,⁴ M. Orlandini,³ P. Romano,⁵ M. Stamatikos^{6,7} and G. Tagliaferri⁴

¹Department of Physics, University of Ferrara, via Saragat 1, I-44122, Ferrara, Italy

²Harvard-Smithsonian Center for Astrophysics, 60 Garden St, Cambridge, MA 02138, USA

³INAF, Istituto di Astrofisica Spaziale e Fisica Cosmica, Bologna, Via Gobetti 101, I-40129 Bologna, Italy

⁴INAF, Osservatorio Astronomico di Brera, Via Bianchi 46, I-23807 Merate (LC), Italy

⁵INAF, Istituto di Astrofisica Spaziale e Fisica Cosmica, Palermo, Via U. La Malfa 153, I-90146, Palermo, Italy

⁶NASA Goddard Space Flight Center, Greenbelt, MD 20771, USA

⁷Department of Physics, Ohio State University, 191 West Woodruff Avenue, Columbus, OH 43210, USA

Accepted 2012 February 14. Received 2012 February 14; in original form 2012 January 23

ABSTRACT

We calculate the average power density spectra (PDSs) of 244 long gamma-ray bursts detected with the *Swift* Burst Alert Telescope (BAT) in the 15–150 keV band from 2005 January to 2011 August. For the first time we derived the average PDS in the source-rest frame of 97 gamma-ray bursts (GRBs) with known redshift. For 49 of them an average PDS was also obtained in a common source-frame energy band to account for the dependence of time profiles on energy. Previous results obtained on Burst and Transient Source Experiment (BATSE) GRBs with unknown redshift showed that the average spectrum in the 25–2000 keV band could be modelled with a power law with a 5/3 index over nearly two decades of frequency with a break at ~ 1 Hz. Depending on the normalization and on the subset of GRBs considered, our results show analogous to steeper slopes (between 1.7 and 2.0) of the power law. However, no clear evidence for the break at ~ 1 Hz was found, although the softer energy band of BAT compared with BATSE might account for that. We instead find a break at lower frequency corresponding to a typical source-rest-frame characteristic time of a few seconds. We furthermore find no significant differences between observer- and source-rest frames. Notably, no distinctive PDS features are found for GRBs with different intrinsic properties of the prompt emission either. Finally, the average PDS of GRBs at higher redshifts shows possibly shallower power-law indices than that of low- z GRBs. It is not clear whether this is due to an evolution with z of the average PDS.

Key words: radiation mechanisms: non-thermal – gamma-ray burst: general.

1 INTRODUCTION

Within the prompt emission of long gamma-ray bursts (GRBs), different degrees of variability are observed over time-scales spanning from milliseconds (Bhat et al. 1992; Walker, Schaefer & Fenimore 2000) up to several seconds. For some GRBs, variability seems to be mostly concentrated on either a unique or more distinct time-scales: a fast component characterized by subsecond variability, superposed to a slow one which comprises the broad pulses and the overall temporal structure (Scargle, Norris & Bonnell 1998; Vetere et al. 2006; Margutti 2009; Gao, Zhang & Zhang 2011). Owing to the variety of GRB time profiles, a simple characterization of GRB temporal variability is still missing. Despite some

claims on occasional events, no unambiguous evidence for coherent pulsations has been found (e.g. Cenko et al. 2010; De Luca et al. 2010). In principle, a better characterization of variability can help to constrain the radiation mechanism and dissipation processes responsible for the burst itself, which is yet one of the least understood aspects of the overall GRB phenomenon (e.g. see the reviews by Ghisellini 2011; Zhang 2011). Theoretical interpretations of the fast and slow components have already been put forward: e.g. in the context of a relativistic jet making its way out through the stellar envelope, the slow component arises from the propagation through the star, while the fast component keeps track of the inner engine activity (Morsony, Lazzati & Begelman 2010). This could be the formation of a hyperaccreting black hole (e.g. MacFayden & Woosley 1999; Kawanaka & Kohri 2011). Alternatively, in the internal-collision-induced magnetic reconnection and turbulence

*E-mail: guidorzi@fe.infn.it

(ICMART) model the inner engine would be responsible for the slow variability, while the fast term is due to relativistic magnetic turbulence taking place in the region where the burst itself is produced (Zhang & Yan 2011).

The study of the Fourier power density spectrum (PDS) provides important clues on the timing properties of astrophysical sources. Fast-Fourier transform (FFT) techniques allow us to discover features like periodic or quasi-periodic pulsations, and to study the continuum or red noise connected with some aperiodic correlated variability in the time series (e.g. van der Klis 1989; Israel & Stella 1996). Beloborodov, Stern & Svensson (1998, 2000, hereafter, BSS98 and BSS00) studied the average PDS of hundreds of GRBs detected with Burst and Transient Source Experiment (BATSE; Paciesas et al. 1999) in the 25–2000 keV energy band and found that it can be described by a power law $f^{-\alpha}$ with $\alpha \sim 5/3$ over almost two decades in frequency, from $\sim 10^{-2}$ to ~ 1 Hz. Above 1 Hz the PDS has a sharp break and steepens significantly. They also observed the same behaviour in the PDS of some individual, long and bright GRBs. Similar results were also obtained on a smaller sample of GRBs detected with *INTEGRAL* (Ryde et al. 2003). However, this investigation has never been done in the source-rest frame due to the poor number of GRBs with known distance observed with past experiments. Instead, it is important to perform this analysis in the source-rest frame, because the observed time profiles are affected by different effects, such as time dilation (Norris et al. 1994), and narrowing of pulses at different energies (Fenimore et al. 1995; Norris et al. 1996), which do depend on redshift. As a consequence, average temporal properties might be affected. As suggested by BSS98, the 5/3 power law is observed in hydrodynamics in the Kolmogorov spectrum of velocity fluctuations within a medium characterized by fully developed turbulence. Within the GRB outflow, the relativistic aberration of light makes the radiation very sensitive to the velocity direction of the emitting blob, and this could link the velocity spectrum with the observed PDS (Narayan & Kumar 2009).

In the context of the internal shock model (Rees & Mészáros 1994), Panaitescu, Spada & Mészáros (1999) and Spada, Panaitescu & Mészáros (2000) used the observed 5/3 slope to constrain the parameters’ space of the wind ejection features which determine the dynamics and optical thickness of the wind of relativistic shells colliding with each other. In addition, assuming that GRB central engines are powered by neutrino-cooled accretion flows, the expected variability can be characterized by a power-law PDS with an index ranging between 1.7 and 2.0 in the 0.1–100 Hz range (Carballido & Lee 2011).

As also pointed out by BSS98, the operation of averaging out hundreds of PDSs of different GRB light curves relies on the assumption that different GRBs are different realizations of the same stochastic process. It is therefore important to study the distribution of the power at each frequency bin for a given sample of GRBs, and to see whether the nature of the distribution depends on frequency.

In this work we carry out an analogous study on the average PDS of different sets of GRBs detected in the 15–150 keV energy band with the Burst Alert Telescope (BAT; Barthelmy et al. 2005) aboard the *Swift* satellite (Gehrels et al. 2004). In addition to being an independent data set obtained with a very different detector, unlike for previous GRB catalogues a significant fraction (~ 30 per cent) of *Swift* GRBs have a measured redshift. This allowed us to carry out the same investigation in the source-rest frame, and to test whether GRBs with different intrinsic properties of the prompt emission also exhibit systematically different PDSs. The paper is organized as follows: Section 2 describes the data selection and analysis.

Results are presented in Section 3, followed by a discussion in Section 4.

2 DATA ANALYSIS

2.1 Data selection

We initially started with a sample of 582 GRBs detected and covered by BAT in burst mode from 2005 January to 2011 August. All the ground-discovered GRBs were excluded to ensure homogeneity of the sample of mask-weighted, background-subtracted light curves with high-time resolution. We selected the long bursts by requiring $T_{90} > 3$ s, where T_{90} were taken from the corresponding BAT refined Gamma-ray Coordinates Network circulars, or from the second BAT catalogue (Sakamoto et al. 2011) when not available. Short GRBs with long extended emission with $T_{90} > 3$ s (Sakamoto et al. 2011) were excluded. After calculating the PDS for GRBs with different peak rates, we rejected those with a poor signal-to-noise (S/N) ratio by setting a threshold on the peak rate of 0.1 count s^{-1} per fully illuminated detector for an equivalent on-axis source. Peak rates were calculated on variable time-scales, from a minimum value of 64 ms. At this stage we ended up with 313 GRBs. For these GRBs we extracted the 64-ms mask-weighted light curve in the 15–150 keV energy band. To this aim, the BAT event files were retrieved and processed with the *HEASOFT* package (v6.11) following the BAT team threads.¹ Mask-weighted light curves were extracted using the ground-refined coordinates provided by the BAT team for each burst through the tool *BATBINEVT*. The BAT detector quality map of each GRB was obtained by processing the next earlier enable/disable map of the detectors. The resulting light curves are expressed as background-subtracted count rates per fully illuminated detector for an equivalent on-axis source. The count rates are normally distributed, and the corresponding σ values are also derived as the relative uncertainties. Consistent results are obtained by using the *BATGRBPRODUCT* script.

Finally, each noise-subtracted PDS (Section 2.3) had its frequency bins grouped so as to fulfil a 3σ criterion. We finally excluded all the GRBs whose PDS consisted of less than four grouped bins. We ended up with 244 GRBs in the observer frame, which hereafter will be referred to as the full sample (Table 1). For these GRBs we also extracted the light curves in two energy channels: 15–50 and 50–150 keV. The aim is to study how the PDS results compare at different energies.

2.2 Subsamples with known redshift

For 150 GRBs of the initial sample with $T_{90} > 3$ s the redshift z is known. We therefore extracted the corresponding 15–150 keV light curves by using a common source-rest-frame bin time of 8 ms. We recalculated the peak rate of the source-rest-frame light curves and applied the same filtering as above, i.e. a threshold to the peak rate, and a minimum number of grouped frequency bins in the noise-subtracted PDS. We ended up with a sample of 97 GRBs with known redshift. Hereafter, we refer to this as the z -silver sample (Table 2).

We also wanted to account for the different rest-frame energy passbands, so we selected a common source-frame energy band as a result of a trade-off between the need for a sufficiently broad-band so as to collect enough photons, and collecting as many GRBs

¹ http://swift.gsfc.nasa.gov/docs/swift/analysis/threads/bat_threads.html

Table 1. The full sample including 244 GRBs in the observer frame.

GRB	t_{start}^a (s)	t_{stop}^a (s)	Log(count fluence) (count det ⁻¹)	Log(peak rate) (count s ⁻¹ det ⁻¹)	T_{90}^a (s)
050117	-203.8	302.7	1.155 ± 0.007	-0.486 ± 0.029	200.0
050124	-3.7	6.6	0.265 ± 0.015	-0.098 ± 0.033	4.1
050128	-37.3	52.8	0.851 ± 0.015	0.158 ± 0.042	13.8
050219A	-30.3	47.0	0.772 ± 0.011	-0.357 ± 0.028	23.0
050219B	-96.1	106.8	1.354 ± 0.010	0.584 ± 0.028	27.0
050306	-188.1	302.8	1.212 ± 0.015	-0.362 ± 0.041	158.4
050315	-179.8	191.6	0.795 ± 0.015	-0.673 ± 0.037	40.0
050319	-160.0	187.0	0.406 ± 0.030	-0.767 ± 0.043	10.0
050326	-49.2	68.9	1.120 ± 0.005	0.284 ± 0.018	29.5
050401	-43.5	64.8	1.105 ± 0.014	0.176 ± 0.030	33.0
050418	-92.8	163.9	0.936 ± 0.012	-0.339 ± 0.022	83.0
050502B	-34.6	20.7	-0.085 ± 0.031	-0.616 ± 0.034	17.5
050505	-63.8	97.3	0.550 ± 0.028	-0.684 ± 0.042	60.0
050525A	-12.3	25.1	1.416 ± 0.002	0.829 ± 0.007	5.2
050603	-26.4	41.7	1.078 ± 0.013	0.846 ± 0.027	12.0
050607	-19.0	37.3	0.057 ± 0.027	-0.902 ± 0.041	26.5
050701	-10.1	33.0	0.411 ± 0.011	-0.420 ± 0.026	40.0
050713A	-112.6	223.9	0.911 ± 0.012	-0.211 ± 0.024	70.0
050713B	-109.7	230.4	0.875 ± 0.032	-0.717 ± 0.050	75.0
050715	-150.0	224.0	0.529 ± 0.024	-0.843 ± 0.039	52.0
050716	-93.8	147.1	0.979 ± 0.013	-0.608 ± 0.030	69.0
050717	-89.0	178.1	0.973 ± 0.008	0.065 ± 0.038	86.0
050801	-6.2	12.8	-0.289 ± 0.034	-0.675 ± 0.039	20.0
050803	-24.2	234.5	0.573 ± 0.022	-0.790 ± 0.045	85.0
050820B	-14.6	29.9	0.528 ± 0.008	-0.271 ± 0.021	13.0
050822	-65.0	206.8	0.732 ± 0.022	-0.593 ± 0.037	102.0
050827	-69.3	76.1	0.530 ± 0.019	-0.617 ± 0.031	49.0
050911	-17.2	32.1	-0.273 ± 0.073	-0.538 ± 0.055	16.0
050915B	-50.0	98.4	0.822 ± 0.010	-0.537 ± 0.028	40.0
050922C	-8.1	9.1	0.411 ± 0.010	0.050 ± 0.025	5.0
051006	-28.7	49.8	0.396 ± 0.029	-0.346 ± 0.065	26.0
051111	-60.7	103.1	0.797 ± 0.011	-0.377 ± 0.029	47.0
051113	-130.2	165.1	0.664 ± 0.030	-0.536 ± 0.046	94.0
051227	-34.2	68.7	-0.061 ± 0.044	-0.839 ± 0.051	8.0
060105	-100.0	153.4	1.393 ± 0.004	0.083 ± 0.028	55.0
060110	-27.4	50.4	0.462 ± 0.013	-0.560 ± 0.024	17.0
060111B	-61.6	117.3	0.379 ± 0.034	-0.726 ± 0.048	59.0
060115	-118.1	224.4	0.546 ± 0.021	-0.993 ± 0.034	142.0
060117	-28.8	52.1	1.502 ± 0.003	0.867 ± 0.017	16.0
060204B	-166.5	264.6	0.703 ± 0.017	-0.758 ± 0.032	134.0
060206	-11.4	21.8	0.211 ± 0.013	-0.406 ± 0.018	7.0
060210	-299.8	302.3	1.093 ± 0.015	-0.349 ± 0.041	46.0
060223A	-14.1	22.2	0.058 ± 0.027	-0.782 ± 0.039	11.0
060223B	-17.7	16.6	0.417 ± 0.012	-0.280 ± 0.038	10.2
060306	-63.8	124.1	0.560 ± 0.020	0.022 ± 0.028	61.0
060312	-100.5	118.2	0.597 ± 0.015	-0.706 ± 0.029	43.0
060322	-239.2	477.8	0.915 ± 0.017	-0.606 ± 0.025	213.0
060403	-37.0	55.5	0.306 ± 0.020	-0.904 ± 0.031	30.0
060413	-60.0	320.0	0.846 ± 0.011	-0.900 ± 0.024	150.0
060418	-171.4	285.8	1.160 ± 0.009	0.073 ± 0.038	52.0
060421	-16.4	24.5	0.287 ± 0.015	-0.397 ± 0.027	11.0
060424	-58.0	59.4	0.109 ± 0.042	-0.521 ± 0.049	37.0
060428A	-54.8	89.9	0.456 ± 0.017	-0.571 ± 0.026	39.4
060502A	-29.1	41.5	0.555 ± 0.013	-0.685 ± 0.021	33.0
060507	-202.8	380.3	0.916 ± 0.017	-0.840 ± 0.036	185.0
060510A	-23.3	29.5	1.229 ± 0.018	0.422 ± 0.037	21.0
060526	-239.2	518.0	0.432 ± 0.042	-0.639 ± 0.043	13.8
060607A	-126.1	214.6	0.665 ± 0.015	-0.752 ± 0.020	100.0
060607B	-30.5	62.0	0.425 ± 0.025	-0.807 ± 0.050	31.0
060614	-166.2	327.7	1.599 ± 0.004	0.441 ± 0.036	102.0
060707	-114.9	86.3	0.496 ± 0.027	-0.930 ± 0.041	68.0
060708	-5.8	11.8	-0.049 ± 0.018	-0.573 ± 0.034	9.8

Table 1 – *continued*

GRB	t_{start}^a (s)	t_{stop}^a (s)	Log(Count fluence) (count det $^{-1}$)	Log(peak rate) (count s $^{-1}$ det $^{-1}$)	T_{90}^a (s)
060714	−134.2	233.6	0.738 ± 0.021	-0.746 ± 0.039	115.0
060719	−59.9	119.6	0.431 ± 0.020	-0.529 ± 0.034	55.0
060813	−28.2	55.7	0.923 ± 0.006	0.054 ± 0.012	14.9
060814	−74.9	384.9	1.386 ± 0.004	-0.031 ± 0.015	146.0
060825	−10.2	14.5	0.269 ± 0.012	-0.438 ± 0.026	8.1
060904A	−60.0	208.1	1.133 ± 0.005	-0.130 ± 0.023	80.0
060904B	−173.7	347.0	0.453 ± 0.036	-0.467 ± 0.031	192.0
060908	−29.3	32.2	0.606 ± 0.012	-0.305 ± 0.033	19.3
060912A	−5.5	10.3	0.381 ± 0.013	0.049 ± 0.021	5.0
060927	−24.7	47.0	0.325 ± 0.017	-0.404 ± 0.023	22.6
061004	−5.1	12.5	0.032 ± 0.016	-0.399 ± 0.027	6.2
061007	−39.9	357.9	1.802 ± 0.002	0.431 ± 0.023	75.0
061019	−239.5	64.0	0.683 ± 0.058	-0.700 ± 0.056	191.0
061021	−54.5	109.2	0.673 ± 0.012	-0.059 ± 0.018	46.0
061121	−135.1	268.2	1.372 ± 0.003	0.546 ± 0.014	81.0
061126	−86.2	156.8	0.998 ± 0.009	0.147 ± 0.017	191.0
061202	9.8	196.2	0.574 ± 0.014	-0.656 ± 0.028	91.0
061222A	−113.5	219.6	1.131 ± 0.006	0.270 ± 0.019	72.0
070103	−18.2	37.1	-0.191 ± 0.047	-0.676 ± 0.064	19.0
070107	−24.0	662.2	0.902 ± 0.015	-0.637 ± 0.026	333.8
070220	−187.1	345.9	1.216 ± 0.007	-0.098 ± 0.020	129.0
070306	−239.2	487.7	0.991 ± 0.015	-0.295 ± 0.019	210.0
070318	−63.9	125.6	0.628 ± 0.013	-0.624 ± 0.024	63.0
070328	−90.0	227.2	1.126 ± 0.006	-0.256 ± 0.020	69.0
070411	−124.1	197.7	0.704 ± 0.016	-0.948 ± 0.035	101.0
070419B	−239.9	400.0	1.118 ± 0.008	-0.765 ± 0.023	236.5
070420	−187.4	230.4	1.360 ± 0.010	-0.093 ± 0.026	77.0
070427	−11.0	23.8	0.159 ± 0.015	-0.716 ± 0.038	11.0
070508	−46.6	73.1	1.464 ± 0.002	0.572 ± 0.015	20.9
070521	−70.3	97.7	1.096 ± 0.006	0.060 ± 0.022	37.9
070529	−115.9	237.8	0.638 ± 0.033	-0.659 ± 0.071	109.0
070612A	−239.0	514.2	1.227 ± 0.018	-0.805 ± 0.030	370.0
070616	−89.9	963.1	1.528 ± 0.004	-0.563 ± 0.029	402.0
070621	−45.5	77.0	0.845 ± 0.011	-0.449 ± 0.038	33.3
070628	−76.2	59.0	0.765 ± 0.016	-0.264 ± 0.017	39.1
070704	−239.0	732.8	0.999 ± 0.013	-0.592 ± 0.017	380.0
070721B	−239.4	542.7	0.757 ± 0.025	-0.720 ± 0.036	340.0
070808	−28.9	55.2	0.265 ± 0.027	-0.573 ± 0.036	32.0
070911	−283.5	302.8	1.347 ± 0.005	-0.210 ± 0.026	162.0
070917	−11.4	22.6	0.489 ± 0.009	0.054 ± 0.016	7.3
071001	−54.6	110.7	0.208 ± 0.031	-0.985 ± 0.046	58.5
071003	−182.6	342.7	1.036 ± 0.014	-0.139 ± 0.024	150.0
071010B	−75.6	77.1	0.861 ± 0.007	-0.111 ± 0.012	35.7
071011	−64.7	119.3	0.495 ± 0.029	-0.714 ± 0.056	61.0
071020	−12.8	16.9	0.507 ± 0.007	0.119 ± 0.018	4.2
071025	−131.5	383.7	1.067 ± 0.009	-0.773 ± 0.028	109.0
071117	−5.0	9.4	0.414 ± 0.010	0.057 ± 0.023	6.6
080205	−121.4	217.1	0.523 ± 0.027	-0.899 ± 0.052	106.5
080210	−35.0	39.8	0.423 ± 0.018	-0.831 ± 0.029	45.0
080229A	−69.7	132.4	1.068 ± 0.010	0.177 ± 0.039	64.0
080310	−84.0	659.5	0.676 ± 0.025	-0.953 ± 0.047	365.0
080319B	−69.6	62.2	2.057 ± 0.001	0.792 ± 0.018	125.0
080319C	−14.3	27.3	0.591 ± 0.013	-0.186 ± 0.034	34.0
080328	−115.9	225.1	1.036 ± 0.010	-0.277 ± 0.041	90.6
080409	−10.0	20.4	-0.205 ± 0.054	-0.481 ± 0.043	20.2
080411	−78.3	155.9	1.647 ± 0.002	0.743 ± 0.007	56.0
080413A	−48.2	97.4	0.734 ± 0.011	-0.168 ± 0.015	46.0
080413B	−6.9	11.0	0.627 ± 0.011	0.280 ± 0.021	8.0
080430	−20.4	40.1	0.360 ± 0.015	-0.472 ± 0.022	16.2
080503	−90.8	181.6	0.487 ± 0.023	-0.564 ± 0.063	170.0
080602	−91.8	149.3	0.687 ± 0.029	-0.326 ± 0.045	74.0
080603B	−67.5	135.4	0.639 ± 0.012	-0.226 ± 0.028	60.0

Table 1 – continued

GRB	t_{start}^a (s)	t_{stop}^a (s)	Log(Count fluence) (count det ⁻¹)	Log(peak rate) (count s ⁻¹ det ⁻¹)	T_{90}^a (s)
080605	-39.4	63.1	1.297 ± 0.004	0.505 ± 0.023	20.0
080607	-157.2	292.3	1.556 ± 0.006	0.577 ± 0.028	79.0
080613B	-86.4	157.2	0.946 ± 0.007	-0.224 ± 0.044	105.0
080623	-8.7	16.0	0.181 ± 0.027	-0.488 ± 0.059	15.2
080714	-30.9	51.2	0.608 ± 0.014	-0.252 ± 0.024	33.0
080721	-34.6	39.2	1.264 ± 0.013	0.513 ± 0.041	16.2
080725	-50.9	55.9	0.715 ± 0.013	-0.596 ± 0.022	120.0
080727B	-9.6	18.5	0.648 ± 0.007	0.114 ± 0.022	8.6
080727C	-113.9	222.3	0.924 ± 0.010	-0.519 ± 0.024	79.7
080804	-33.5	68.6	0.713 ± 0.018	-0.444 ± 0.033	34.0
080805	-88.7	170.3	0.644 ± 0.014	-0.846 ± 0.027	78.0
080810	-122.6	220.2	0.860 ± 0.012	-0.499 ± 0.034	106.0
080903	-61.9	98.0	0.489 ± 0.017	-0.991 ± 0.055	66.0
080905B	-96.1	191.9	0.483 ± 0.032	-0.759 ± 0.045	128.0
080906	-239.4	267.3	0.830 ± 0.015	-0.932 ± 0.022	147.0
080915B	-4.0	6.4	0.259 ± 0.012	0.025 ± 0.019	3.9
080916A	-76.4	146.2	0.839 ± 0.008	-0.461 ± 0.016	60.0
080928	-131.5	400.0	0.675 ± 0.020	-0.495 ± 0.031	280.0
081008	-239.6	338.4	0.876 ± 0.013	-0.797 ± 0.024	185.5
081102	-54.7	54.2	0.551 ± 0.023	-0.756 ± 0.037	63.0
081109	-109.0	169.0	0.790 ± 0.011	-0.791 ± 0.019	190.0
081126	-85.3	106.9	0.723 ± 0.012	-0.302 ± 0.021	54.0
081128	-80.0	153.5	0.681 ± 0.015	-0.787 ± 0.037	100.0
081203A	-141.7	255.4	1.052 ± 0.008	-0.318 ± 0.032	294.0
081210	-109.9	287.1	0.546 ± 0.025	-0.453 ± 0.028	146.0
081221	-102.4	205.4	1.509 ± 0.003	0.375 ± 0.013	33.5
081222	-37.1	72.7	0.922 ± 0.005	0.019 ± 0.012	24.0
090102	-12.4	85.2	1.013 ± 0.017	0.022 ± 0.053	27.0
090113	-9.4	18.7	0.112 ± 0.020	-0.367 ± 0.033	9.1
090123	-120.0	178.3	0.658 ± 0.023	-0.738 ± 0.045	131.0
090129	-26.0	51.8	0.630 ± 0.010	-0.297 ± 0.020	17.5
090201	-118.9	210.7	1.660 ± 0.007	0.356 ± 0.029	83.0
090301	-93.6	85.1	1.515 ± 0.003	0.418 ± 0.016	41.0
090401A	-14.0	292.1	1.245 ± 0.007	0.189 ± 0.020	112.0
090401B	-140.5	281.0	1.194 ± 0.006	0.558 ± 0.012	183.0
090404	-119.6	154.0	0.808 ± 0.011	-0.586 ± 0.032	84.0
090410	-76.0	328.2	0.962 ± 0.009	-0.438 ± 0.033	165.0
090418A	-69.6	124.7	0.854 ± 0.013	-0.545 ± 0.046	56.0
090422	-8.1	16.0	-0.308 ± 0.051	-0.411 ± 0.046	8.5
090423	-10.7	22.3	0.105 ± 0.019	-0.679 ± 0.035	10.3
090424	-83.2	164.4	1.522 ± 0.005	0.948 ± 0.013	48.0
090509	-239.3	300.0	0.731 ± 0.038	-0.678 ± 0.062	335.0
090516	-231.2	447.1	1.114 ± 0.031	-0.564 ± 0.057	210.0
090518	-5.0	6.4	-0.113 ± 0.021	-0.527 ± 0.037	6.9
090530	-41.0	81.8	0.266 ± 0.034	-0.260 ± 0.046	48.0
090531B	-55.6	112.0	0.109 ± 0.040	-0.574 ± 0.044	80.0
090618	-214.5	412.3	2.244 ± 0.001	0.657 ± 0.003	113.2
090628	-19.0	15.2	0.058 ± 0.029	-0.728 ± 0.046	20.1
090709A	-236.5	273.5	1.576 ± 0.003	0.030 ± 0.016	89.0
090715B	-239.6	550.0	0.993 ± 0.012	-0.316 ± 0.012	266.0
090812	-99.3	183.9	0.939 ± 0.009	-0.242 ± 0.028	66.7
090813	-7.0	13.9	0.375 ± 0.021	0.182 ± 0.039	7.1
090904A	-96.2	321.8	0.801 ± 0.017	-0.664 ± 0.022	122.0
090904B	-60.0	105.4	1.254 ± 0.013	-0.382 ± 0.081	47.0
090912	-139.6	276.2	0.889 ± 0.021	-0.774 ± 0.036	144.0
090926B	-171.2	281.4	1.029 ± 0.012	-0.477 ± 0.021	109.7
090929B	-239.4	380.0	1.025 ± 0.014	-0.190 ± 0.032	360.0
091018	-7.0	13.4	0.497 ± 0.008	0.093 ± 0.012	4.4
091020	-47.1	77.5	0.760 ± 0.012	-0.295 ± 0.019	34.6
091026	-56.0	101.1	0.508 ± 0.023	-0.514 ± 0.034	41.6
091029	-43.1	82.2	0.684 ± 0.009	-0.641 ± 0.021	39.2

Table 1 – *continued*

GRB	t_{start}^a (s)	t_{stop}^a (s)	Log(Count fluence) (count det $^{-1}$)	Log(peak rate) (count s $^{-1}$ det $^{-1}$)	T_{90}^a (s)
091102	−6.9	13.0	$−0.088 \pm 0.025$	$−0.537 \pm 0.046$	6.6
091127	−10.5	20.1	1.186 ± 0.011	0.844 ± 0.030	7.1
091130B	−117.4	227.2	0.522 ± 0.024	$−0.868 \pm 0.038$	112.5
091208A	−30.8	61.3	0.329 ± 0.020	$−0.613 \pm 0.023$	29.1
091208B	−10.4	21.6	0.678 ± 0.019	0.368 ± 0.038	14.9
091221	−119.0	118.2	1.002 ± 0.009	$−0.407 \pm 0.020$	68.5
100111A	−15.3	16.2	0.087 ± 0.023	$−0.630 \pm 0.033$	12.9
100119A	−48.4	47.6	1.279 ± 0.012	$−0.030 \pm 0.025$	23.8
100212A	−231.7	316.8	0.359 ± 0.048	$−0.430 \pm 0.036$	136.0
100413A	−207.1	422.4	0.958 ± 0.016	$−0.754 \pm 0.091$	191.0
100423A	−118.4	156.0	1.120 ± 0.008	0.179 ± 0.030	160.0
100425A	−39.9	74.0	0.108 ± 0.050	$−0.775 \pm 0.046$	37.0
100504A	−116.3	210.3	0.620 ± 0.022	$−0.704 \pm 0.029$	97.3
100522A	−35.8	71.1	0.576 ± 0.015	0.076 ± 0.032	35.3
100606A	−75.1	150.3	0.888 ± 0.016	$−0.324 \pm 0.044$	480.0
100615A	−47.1	94.4	0.962 ± 0.006	$−0.149 \pm 0.019$	39.0
100619A	−108.5	212.6	0.883 ± 0.011	$−0.240 \pm 0.015$	97.5
100621A	−103.6	190.5	1.580 ± 0.002	0.202 ± 0.008	63.6
100704A	−217.4	397.4	0.992 ± 0.011	$−0.251 \pm 0.017$	197.5
100725A	−86.5	168.8	0.512 ± 0.019	$−0.999 \pm 0.052$	141.0
100725B	−222.9	436.2	1.078 ± 0.012	$−0.525 \pm 0.022$	200.0
100727A	−134.8	102.7	0.375 ± 0.024	$−0.811 \pm 0.034$	84.0
100728A	−110.0	723.0	1.736 ± 0.002	$−0.112 \pm 0.024$	198.5
100802A	−200.0	936.7	0.836 ± 0.019	$−0.972 \pm 0.033$	487.0
100814A	−235.0	460.6	1.154 ± 0.008	$−0.484 \pm 0.013$	174.5
100823A	−20.7	38.8	$−0.087 \pm 0.038$	$−0.949 \pm 0.042$	16.9
100902A	−89.9	859.1	0.786 ± 0.024	$−0.984 \pm 0.029$	428.8
100906A	−130.6	261.0	1.283 ± 0.005	0.104 ± 0.016	114.4
100924A	−79.4	155.5	1.116 ± 0.010	$−0.192 \pm 0.032$	96.0
101008A	−10.5	15.5	0.051 ± 0.028	$−0.494 \pm 0.063$	104.0
101011A	−36.9	73.1	0.307 ± 0.023	$−0.701 \pm 0.041$	71.5
101017A	−116.9	217.5	1.416 ± 0.004	0.176 ± 0.035	70.0
101023A	−119.9	225.7	1.630 ± 0.005	0.450 ± 0.008	80.8
101024A	−20.1	39.7	0.423 ± 0.014	0.005 ± 0.024	18.7
101030A	−183.9	148.7	0.733 ± 0.021	$−0.948 \pm 0.027$	92.0
101117B	−3.8	7.6	0.232 ± 0.015	$−0.082 \pm 0.037$	5.2
110102A	−100.0	617.4	1.417 ± 0.005	0.074 ± 0.017	264.0
110106B	−26.0	44.7	0.544 ± 0.019	$−0.484 \pm 0.049$	24.8
110119A	−230.7	438.5	1.059 ± 0.009	$−0.397 \pm 0.030$	208.0
110201A	−10.1	19.4	$−0.019 \pm 0.021$	$−0.742 \pm 0.043$	13.0
110205A	−239.0	727.0	1.439 ± 0.005	$−0.279 \pm 0.030$	257.0
110207A	−70.6	141.2	0.392 ± 0.025	$−0.219 \pm 0.041$	80.3
110213A	−53.8	48.0	0.979 ± 0.018	0.092 ± 0.033	48.0
110315A	−161.8	127.0	0.846 ± 0.015	$−0.685 \pm 0.048$	77.0
110318A	−24.3	27.1	0.892 ± 0.010	0.002 ± 0.017	16.0
110319A	−23.9	47.8	0.548 ± 0.010	$−0.592 \pm 0.019$	19.3
110402A	−31.6	74.2	0.709 ± 0.030	0.312 ± 0.060	60.9
110411A	−106.8	182.8	0.826 ± 0.012	$−0.819 \pm 0.026$	80.3
110414A	−205.0	304.8	0.758 ± 0.031	$−0.997 \pm 0.039$	152.0
110420A	−24.6	50.1	1.043 ± 0.009	0.174 ± 0.018	11.8
110422A	−55.3	77.2	1.738 ± 0.003	0.590 ± 0.013	25.9
110503A	−11.1	17.0	1.143 ± 0.009	0.579 ± 0.021	10.0
110519A	−34.9	58.2	0.877 ± 0.009	$−0.274 \pm 0.016$	27.2
110610A	−76.6	123.0	0.882 ± 0.009	$−0.270 \pm 0.022$	46.4
110625A	−157.3	280.8	1.641 ± 0.008	0.828 ± 0.025	44.5
110709A	−64.0	116.9	1.187 ± 0.004	$−0.046 \pm 0.027$	44.7
110715A	−19.2	35.0	1.266 ± 0.003	0.881 ± 0.009	13.0
110731A	−26.4	49.7	0.915 ± 0.006	0.245 ± 0.016	38.8
110801A	−239.2	792.5	0.976 ± 0.017	$−0.813 \pm 0.056$	385.0

Note: The PDS is calculated in the time interval reported.

^aReferred to the BAT trigger time and calculated in the observer frame.

Table 2. The z -silver sample including 97 GRBs.

GRB	z	t_{start}^a (s)	t_{stop}^a (s)	Log(count fluence) (count det $^{-1}$)	Log(peak rate) b (count s $^{-1}$ det $^{-1}$)
050315	1.949	−61.0	65.0	0.785 ± 0.014	-0.226 ± 0.032
050318	1.440	−13.4	13.3	0.375 ± 0.015	0.051 ± 0.023
050319	3.240	−37.7	44.1	0.396 ± 0.029	-0.186 ± 0.031
050401	2.900	−11.1	16.6	1.094 ± 0.014	0.739 ± 0.031
050505	4.270	−12.1	18.5	0.549 ± 0.027	-0.008 ± 0.037
050525A	0.606	−7.7	15.6	1.413 ± 0.001	1.042 ± 0.007
050603	2.821	−6.9	10.9	1.062 ± 0.013	1.360 ± 0.021
050730	3.967	−42.4	57.6	0.673 ± 0.019	-0.565 ± 0.032
050820A	2.612	−68.0	83.0	0.763 ± 0.017	0.021 ± 0.021
050922C	2.198	−2.5	2.9	0.405 ± 0.009	0.507 ± 0.020
051111	1.550	−23.8	40.4	0.789 ± 0.010	-0.087 ± 0.018
060115	3.530	−26.1	49.5	0.543 ± 0.020	-0.372 ± 0.028
060206	4.048	−2.3	4.3	0.201 ± 0.013	0.273 ± 0.016
060210	3.910	−61.1	61.6	1.082 ± 0.014	0.212 ± 0.031
060223A	4.410	−2.6	4.1	0.057 ± 0.025	-0.069 ± 0.033
060418	1.489	−68.9	114.8	1.149 ± 0.009	0.414 ± 0.025
060502A	1.510	−11.6	16.5	0.547 ± 0.013	-0.300 ± 0.020
060510B	4.900	−40.5	71.5	0.886 ± 0.012	-0.549 ± 0.027
060526	3.210	−56.8	123.0	0.415 ± 0.041	-0.070 ± 0.036
060607A	3.082	−30.9	52.5	0.658 ± 0.014	-0.154 ± 0.018
060614	0.125	−147.7	291.3	1.596 ± 0.004	0.457 ± 0.035
060707	3.430	−25.9	19.5	0.482 ± 0.026	-0.295 ± 0.042
060714	2.710	−36.2	62.9	0.728 ± 0.020	-0.207 ± 0.036
060814	0.840	−40.7	209.2	1.379 ± 0.004	0.225 ± 0.014
060904B	0.703	−102.0	203.7	0.429 ± 0.036	-0.262 ± 0.027
060906	3.685	−10.2	11.7	0.644 ± 0.017	-0.062 ± 0.040
060908	1.884	−10.2	11.2	0.601 ± 0.011	0.110 ± 0.029
060912A	0.937	−2.8	5.3	0.373 ± 0.012	0.332 ± 0.021
060927	5.467	−3.8	7.3	0.319 ± 0.016	0.352 ± 0.024
061007	1.262	−17.7	158.2	1.789 ± 0.002	0.696 ± 0.013
061021	0.346	−40.6	81.1	0.671 ± 0.011	0.061 ± 0.018
061121	1.314	−58.4	115.9	1.366 ± 0.003	0.865 ± 0.009
061126	1.159	−39.9	72.6	0.988 ± 0.009	0.456 ± 0.016
061222A	2.088	−36.8	71.1	1.124 ± 0.006	0.661 ± 0.012
070306	1.496	−95.8	195.4	0.993 ± 0.014	0.092 ± 0.017
070318	0.836	−34.8	68.4	0.623 ± 0.012	-0.388 ± 0.021
070411	2.954	−31.4	50.0	0.698 ± 0.015	-0.379 ± 0.029
070529	2.500	−33.1	67.9	0.605 ± 0.034	-0.195 ± 0.071
070612A	0.617	−147.8	318.0	1.225 ± 0.017	-0.611 ± 0.031
070721B	3.626	−51.8	117.3	0.745 ± 0.025	-0.081 ± 0.034
071003	1.604	−70.1	131.6	1.030 ± 0.013	0.255 ± 0.021
071010B	0.947	−38.8	39.6	0.862 ± 0.007	0.166 ± 0.011
071020	2.145	−4.1	5.4	0.499 ± 0.007	0.575 ± 0.015
071117	1.331	−2.2	4.0	0.409 ± 0.010	0.403 ± 0.018
080210	2.641	−9.6	10.9	0.414 ± 0.017	-0.272 ± 0.030
080310	2.430	−24.5	192.3	0.677 ± 0.024	-0.441 ± 0.037
080319B	0.937	−35.9	32.1	2.046 ± 0.001	0.876 ± 0.008
080319C	1.950	−4.9	9.3	0.579 ± 0.012	0.244 ± 0.028
080330	1.510	−23.3	46.7	-0.130 ± 0.074	-0.567 ± 0.060
080411	1.030	−38.6	76.8	1.643 ± 0.002	1.047 ± 0.007
080413A	2.433	−14.0	28.4	0.729 ± 0.010	0.355 ± 0.013
080413B	1.100	−3.3	5.2	0.624 ± 0.011	0.586 ± 0.022
080430	0.767	−11.5	22.7	0.370 ± 0.013	-0.235 ± 0.018
080603B	2.690	−18.3	36.7	0.635 ± 0.012	0.257 ± 0.023
080605	1.640	−14.9	23.9	1.290 ± 0.004	0.852 ± 0.015
080607	3.036	−38.9	72.4	1.544 ± 0.005	1.142 ± 0.020
080721	2.591	−9.6	10.9	1.246 ± 0.013	1.014 ± 0.040
080804	2.204	−10.4	21.4	0.699 ± 0.018	-0.028 ± 0.027
080805	1.505	−35.4	68.0	0.641 ± 0.013	-0.481 ± 0.023
080810	3.350	−28.2	50.6	0.854 ± 0.012	0.052 ± 0.037

Table 2 – *continued*

GRB	z	t_{start}^a (s)	t_{stop}^a (s)	Log(Count fluence) (count det $^{-1}$)	Log(peak rate) b (count s $^{-1}$ det $^{-1}$)
080905B	2.374	−28.5	56.9	0.487 ± 0.030	$−0.241 \pm 0.043$
080906	2.130	−76.5	85.4	0.832 ± 0.014	$−0.437 \pm 0.022$
080916A	0.689	−45.3	86.6	0.837 ± 0.008	$−0.240 \pm 0.018$
080928	1.692	−48.9	148.6	0.680 ± 0.019	$−0.076 \pm 0.038$
081008	1.968	−80.7	114.0	0.868 ± 0.013	$−0.335 \pm 0.025$
081028	3.038	−38.9	114.9	0.829 ± 0.014	$−0.696 \pm 0.026$
081222	2.770	−9.8	19.3	0.917 ± 0.005	0.586 ± 0.009
090102	1.547	−4.9	33.4	0.988 ± 0.017	0.404 ± 0.047
090418A	1.608	−26.7	47.8	0.849 ± 0.013	$−0.180 \pm 0.034$
090423	8.100	−1.2	2.5	0.098 ± 0.019	0.272 ± 0.030
090424	0.544	−53.9	106.5	1.515 ± 0.005	1.140 ± 0.012
090516	4.109	−45.3	87.5	1.114 ± 0.029	0.109 ± 0.058
090530	1.280	−18.0	35.8	0.245 ± 0.033	0.017 ± 0.035
090618	0.540	−139.4	267.7	2.239 ± 0.001	0.841 ± 0.004
090715B	3.000	−59.9	137.5	0.984 ± 0.012	0.278 ± 0.012
090812	2.452	−28.8	53.3	0.934 ± 0.009	0.261 ± 0.027
090926B	1.240	−76.5	125.6	1.033 ± 0.011	$−0.128 \pm 0.020$
091018	0.971	−3.5	6.8	0.493 ± 0.007	0.378 ± 0.013
091020	1.710	−17.4	28.6	0.754 ± 0.011	0.115 ± 0.017
091024	1.092	−56.0	92.2	0.962 ± 0.014	$−0.282 \pm 0.028$
091029	2.752	−11.5	21.9	0.681 ± 0.009	$−0.086 \pm 0.018$
091127	0.490	−7.0	13.5	1.178 ± 0.011	0.991 ± 0.025
091208B	1.063	−5.1	10.5	0.671 ± 0.018	0.670 ± 0.037
100425A	1.755	−14.5	26.9	0.092 ± 0.049	$−0.330 \pm 0.048$
100621A	0.542	−67.2	123.5	1.578 ± 0.002	0.389 ± 0.008
100814A	1.440	−96.3	188.8	1.152 ± 0.007	$−0.121 \pm 0.011$
100906A	1.727	−47.9	95.7	1.280 ± 0.005	0.524 ± 0.016
101213A	0.414	−51.2	96.8	0.860 ± 0.014	$−0.464 \pm 0.036$
110106B	0.618	−16.1	27.6	0.538 ± 0.018	$−0.274 \pm 0.047$
110205A	2.200	−74.7	227.2	1.434 ± 0.005	0.190 ± 0.024
110213A	1.460	−21.9	19.5	0.977 ± 0.017	0.479 ± 0.034
110422A	1.770	−20.0	27.9	1.731 ± 0.003	0.995 ± 0.010
110503A	1.613	−4.2	6.5	1.138 ± 0.008	0.985 ± 0.018
110715A	0.820	−10.6	19.2	1.262 ± 0.003	1.129 ± 0.009
110731A	2.830	−6.9	13.0	0.909 ± 0.005	0.793 ± 0.012
110801A	1.858	−83.7	277.3	0.963 ± 0.017	$−0.382 \pm 0.042$
110818A	3.360	−15.9	29.9	0.749 ± 0.020	$−0.148 \pm 0.045$

Note: The PDS is calculated in the time interval reported.

^a Referred to the BAT trigger time and calculated in the source-rest frame.

^b Calculated in the source-rest frame.

as possible. We therefore chose the 66–366 keV energy band (rest frame), which is fully covered by the 15–150 keV BAT passband² for 62 GRBs with $1.4 < z < 3.5$. For these GRBs we re-extracted the corresponding light curves in the common source-rest-frame energy band with a common rest-frame bin time of 4 ms. Applying the same filtering criteria as above we ended up with a final sample of 49 GRBs. Hereafter, this will be referred to as the z -golden sample (Table 3).

Fig. 1 shows the z -golden sample together with the full sample of 244 GRBs in the $\log P - \log F$ plane evaluated in the observer frame, where P is the peak rate and F is the count fluence per fully illuminated detector for an on-axis source. While the two samples have similar P distributions, that with known z seems to be biased against low-fluence GRBs. However, a Kolmogorov–Smirnov (K–S) test yields a 9.7 per cent probability for the two distributions

of being drawn from the same population. The z -golden sample thus is not inconsistent with being an unbiased selection of the full set in the $\log P - \log F$ plane. From Fig. 1 it is also apparent that extrapolating to peak rates below the threshold of $0.1 \text{ count s}^{-1} \text{ det}^{-1}$ would not increase the sample of GRBs with useful S/N, because the fraction of rejected GRBs becomes dominant.

2.3 PDS calculation

The choice of the time interval over which the PDS is most conveniently calculated was driven by the need for covering the overall GRB profile as well as optimizing the S/N. We verified that the overall shape of the PDS does not depend on the particular choice of the time interval, whereas its S/N clearly does. After a number of attempts, we came up with the following choice: first we found the first ($t_1^{(n\sigma)}$) and the last ($t_2^{(n\sigma)}$) time bins whose count rates exceeded the background level at $n\sigma$ ($n \geq 5$). Let $\Delta_{n\sigma} = t_2^{(n\sigma)} - t_1^{(n\sigma)}$ be the duration of this interval. The time interval chosen for the

² We did not consider photons above 150 keV because of the drop in the BAT effective area for such energies (Barthelmy et al. 2005).

Table 3. The z -golden sample including 49 GRBs.

GRB	z	t_{start}^a (s)	t_{stop}^a (s)	Log(count fluence) (count det $^{-1}$)	Log(peak rate) b (count s $^{-1}$ det $^{-1}$)
050315	1.949	−61.0	65.0	0.631 ± 0.017	-0.367 ± 0.036
050319	3.240	−41.1	44.1	0.353 ± 0.031	-0.213 ± 0.042
050401	2.900	−11.1	16.6	1.027 ± 0.015	0.677 ± 0.033
050603	2.821	−6.9	10.9	0.997 ± 0.014	1.212 ± 0.024
050922C	2.198	−2.5	2.9	0.332 ± 0.010	0.471 ± 0.020
051111	1.550	−23.8	40.4	0.655 ± 0.011	-0.172 ± 0.021
060418	1.489	−68.9	114.8	0.959 ± 0.010	0.263 ± 0.029
060502A	1.510	−11.6	16.5	0.400 ± 0.014	-0.353 ± 0.029
060526	3.210	−56.8	123.0	0.386 ± 0.040	-0.113 ± 0.038
060607A	3.082	−30.9	52.5	0.612 ± 0.014	-0.210 ± 0.017
060707	3.430	−25.9	19.5	0.438 ± 0.027	-0.339 ± 0.042
060714	2.710	−36.2	62.9	0.665 ± 0.021	-0.271 ± 0.039
060908	1.884	−10.2	11.2	0.505 ± 0.012	0.044 ± 0.031
061222A	2.088	−36.8	71.1	1.029 ± 0.006	0.592 ± 0.013
070306	1.496	−95.8	195.4	0.800 ± 0.018	-0.090 ± 0.021
070411	2.954	−31.4	50.0	0.631 ± 0.016	-0.363 ± 0.036
070529	2.500	−33.1	67.9	0.561 ± 0.033	-0.250 ± 0.073
071003	1.604	−70.1	131.6	0.887 ± 0.015	0.152 ± 0.022
071020	2.145	−4.1	5.4	0.415 ± 0.008	0.502 ± 0.015
080210	2.641	−9.6	10.9	0.340 ± 0.018	-0.323 ± 0.030
080310	2.430	−20.0	192.3	0.579 ± 0.025	-0.532 ± 0.035
080319C	1.950	−4.9	9.3	0.497 ± 0.013	0.139 ± 0.033
080413A	2.433	−14.0	28.4	0.646 ± 0.011	0.295 ± 0.014
080603B	2.690	−18.3	36.7	0.569 ± 0.012	0.155 ± 0.018
080605	1.640	−14.9	23.9	1.166 ± 0.004	0.782 ± 0.016
080607	3.036	−38.9	72.4	1.472 ± 0.006	1.056 ± 0.022
080721	2.591	−9.6	10.9	1.162 ± 0.014	0.879 ± 0.033
080804	2.204	−10.4	21.4	0.621 ± 0.018	-0.047 ± 0.029
080805	1.505	−35.4	68.0	0.440 ± 0.017	-0.530 ± 0.026
080810	3.350	−28.2	50.6	0.795 ± 0.012	0.000 ± 0.038
080905B	2.374	−28.5	56.9	0.395 ± 0.032	-0.310 ± 0.042
080906	2.130	−76.5	85.4	0.740 ± 0.015	-0.501 ± 0.026
080928	1.692	−48.9	150.0	0.511 ± 0.023	-0.225 ± 0.031
081008	1.968	−80.7	114.0	0.747 ± 0.014	-0.408 ± 0.030
081222	2.770	−9.8	19.3	0.857 ± 0.005	0.523 ± 0.014
090102	1.547	−4.9	33.4	0.865 ± 0.019	0.290 ± 0.053
090418A	1.608	−26.7	47.8	0.721 ± 0.014	-0.252 ± 0.046
090715B	3.000	−59.9	140.0	0.923 ± 0.012	0.221 ± 0.013
090812	2.452	−28.8	53.3	0.862 ± 0.009	0.205 ± 0.027
091020	1.710	−17.4	28.6	0.602 ± 0.013	0.007 ± 0.019
091029	2.752	−11.5	21.9	0.612 ± 0.009	-0.143 ± 0.023
100814A	1.440	−96.3	188.8	0.976 ± 0.008	-0.194 ± 0.012
100906A	1.727	−47.9	95.7	1.118 ± 0.006	0.415 ± 0.017
110205A	2.200	−74.7	227.2	1.331 ± 0.006	0.105 ± 0.026
110213A	1.460	−21.9	19.5	0.770 ± 0.022	0.321 ± 0.040
110422A	1.770	−20.0	27.9	1.634 ± 0.003	0.939 ± 0.013
110503A	1.613	−4.2	6.5	1.028 ± 0.009	0.893 ± 0.020
110731A	2.830	−6.9	13.0	0.841 ± 0.006	0.740 ± 0.013
110801A	1.858	−83.7	277.3	0.804 ± 0.020	-0.555 ± 0.044

Note: The PDS is calculated in the time interval reported.

^aReferred to the BAT trigger time, and calculated in the source-rest frame.

^bCalculated in the source-rest frame.

PDS calculation starts at $t_1^{(n\sigma)} - \Delta_{n\sigma}$ and ends at $t_2^{(n\sigma)} + \Delta_{n\sigma}$. If we had chosen a fixed time interval for all GRBs, thus with a common frequency binning scheme, the S/N of the shortest GRBs would have been worse, due to including additional noise with no signal. In the observer frame the bin time was fixed to 64 ms, while for the source-rest-frame GRBs two rest-frame bin times were used, 4 and 8 ms. We found no notable difference between $n = 5$ and 7, apart from a different S/N in the average PDS, which led us to finally

choose $n = 7$. Tables 1–3 report the time intervals for all GRBs in each GRB sample.

In the full sample the duration of this time interval is found to be three times as long as the GRB duration expressed by its T_{90} . Given that the time interval duration is by construction $3 \Delta_{7\sigma}$, this simply reflects that, on average, $\Delta_{7\sigma}$ does not differ from T_{90} remarkably.

The PDS was obtained through the mixed-radix FFT algorithm implemented within the GNU Scientific Library (Galassi et al.

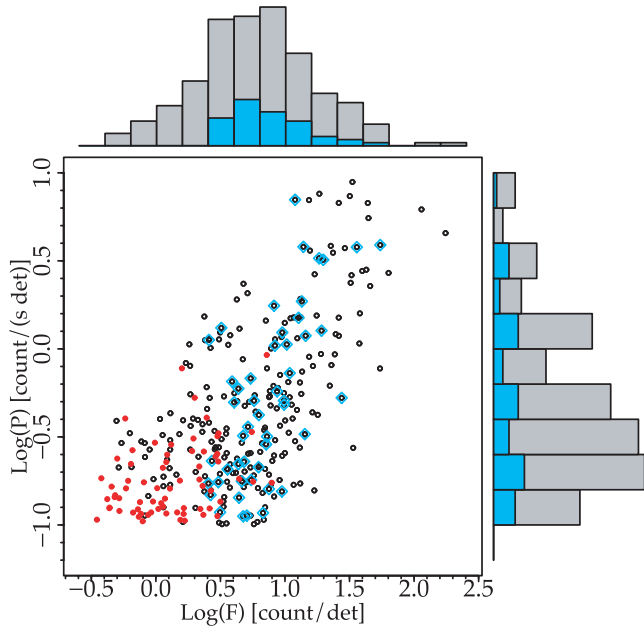


Figure 1. The full set of 244 GRBs selected in the observer frame (empty circles) and the z -golden subset with known z and a common source-rest-frame energy band (diamonds) shown in the peak rate-count fluence plane (observer frame). The filled circles show the GRBs discarded by our filtering procedure because of their poor PDS. The corresponding histograms are also shown along both axes.

2009),³ which does not require the total number of bins to be a power of 2 (Temperton 1983). Each PDS was calculated adopting the Leahy normalization, in which the constant power due to statistical noise has a value of 2 (Leahy et al. 1983). Usually the PDS is calculated from the light curves *not* background subtracted to ensure that counts are Poisson distributed, and consequently the power distribution is known: e.g. in the case of pure statistical noise, the power is χ^2_2 distributed. In the case of BAT data, the background subtraction through the mask weighting technique is not an issue as explained below.

The average PDS of a given sample of GRBs was obtained assuming two different normalizations: (i) the BAT mask-weighted count rates and corresponding errors are normally distributed and there is no evidence for any extra variance (down to a few per cent) in addition to the statistical white noise (Rizzuto et al. 2007). The uncertainties on the power of the individual PDSs were calculated according to Guidorzi (2011). From Parseval's theorem the integral of each individual noise-subtracted PDS yields the net variance, i.e. removed of the statistical noise. In this case each PDS was normalized by its net variance. This normalization is preferable, because all GRBs have equal weights in the average PDS. (ii) Each GRB light curve is normalized by its peak rate, which allows us to make a direct comparison with BSS98 and BSS00. Hereafter, the two cases are referred to as the (net) variance and the peak normalizations, respectively. A possible third normalization based on the count fluence was soon neglected, due to the results on the binned average PDSs, which were statistically poorer and less constraining than for the other normalizations. Using different normalizations allows us to evaluate the effects of this kind of choice.

The statistical noise was removed differently in the two cases: (i) the noise was assumed to be perfectly Poissonian (Rizzuto et al. 2007), and calculated consequently. (ii) It was obtained from fitting the average PDS with a constant at sufficiently high frequencies.

We started from a uniform frequency binning scheme with a step of 0.01 Hz. At $f < 0.01$ Hz we considered two bins, $0.001 \leq f < 0.005$ Hz and $0.005 \leq f < 0.01$ Hz. For each frequency bin and for each individual GRB we calculated the average power. Finally, for each frequency bin we averaged out the power over all the GRBs of a given sample. The average power in each bin is approximately normally distributed with $\sigma = \sigma_p / \sqrt{n}$, where σ_p is the standard deviation of the corresponding power distribution and n the size of the array, i.e. roughly the size of a given GRB sample. Its validity is ensured by the central limit theorem. σ was therefore taken as the uncertainty of the corresponding average power. Finally the frequency bins of the average noise-subtracted PDS were grouped by requiring at least 3σ significance.

2.4 PDS modelling

We modelled the average PDSs with a smoothly broken power law as in equation (1),

$$\text{PDS}(f) = 2^{1/n} F_0 \left[\left(\frac{f}{f_b} \right)^{n\alpha_1} + \left(\frac{f}{f_b} \right)^{n\alpha_2} \right]^{-1/n}, \quad (1)$$

where the following parameters were left free to vary: the break frequency f_b , the value of the PDS at the break frequency F_0 , the two power-law indices α_1 and α_2 ($\alpha_2 > \alpha_1$). Initially, the peakedness parameter n was also left free to vary. However in most cases the data were not sensitive to it, so we fixed $n = 10$ for all cases to ensure a more homogeneous comparison between the best-fitting values obtained over different sets. This choice implies a rather sharp break around f_b .

In Section 3.6 we discuss more in detail how much the results, especially α_2 , depend on this degree of freedom. The best-fitting model is obtained by minimizing the total χ^2 .

3 RESULTS

Table 4 reports the best-fitting parameters of the model in equation (1) for each GRB sample and both normalizations. Parameters' uncertainties are given at 90 per cent confidence level for one parameter of interest.

Fig. 2 displays the average PDS of the full sample for both normalizations as well as their corresponding best-fitting models. The variance-normalized PDS has a best-fitting value of around 1.03 ± 0.05 for α_1 , followed by a break around 3×10^{-2} Hz, above which the slope becomes $\alpha_2 = 1.73^{+0.04}_{-0.03}$. The peak-normalized PDS has a similar value for f_b , and steeper values for the power-law indices: $\alpha_1 = 1.25^{+0.11}_{-0.12}$ and $\alpha_2 = 1.90^{+0.07}_{-0.06}$. The difference ($\alpha_i^{(\text{peak})} - \alpha_i^{(\text{var})}$) in the power-law indices between the two normalizations is found to be in the range 0.1–0.2 for all the GRB subsamples considered, although it is always compatible with zero at 3σ .

The value of α_2 is very similar to the power-law index 1.67 ± 0.02 in the range $0.02 < f < 1$ Hz in the 50–300 keV band found by BSS98, and between 1.50 and 1.72 in the range $0.025 < f < 1$ Hz in the 20–2000 keV band found by BSS00. Very similar results are obtained for the z -silver and golden samples (Figs 3 and 4), apart from the best-fitting values of f_b which are higher in the source-rest frame. This is no wonder, and links to the cosmological time dilation. This is quantified by fitting the average PDS of the z -golden sample in the observer frame: moving from observer- to source-rest

³ <http://www.gnu.org/s/gsl/>

Table 4. Best-fitting parameters of the average PDS for different samples of GRBs.

Sample	Size	α_1	Variance norm.		χ^2/dof	α_1	Peak norm.		χ^2/dof
			f_b (10^{-2} Hz)	α_2			f_b (10^{-2} Hz)	α_2	
Full	244	$1.03^{+0.05}_{-0.05}$	$3.0^{+0.5}_{-0.4}$	$1.73^{+0.04}_{-0.03}$	73.5/63	$1.25^{+0.11}_{-0.12}$	$2.0^{+0.6}_{-0.4}$	$1.90^{+0.07}_{-0.06}$	15.4/21
z-silver	97	$1.01^{+0.07}_{-0.08}$	$6.9^{+1.5}_{-1.2}$	$1.77^{+0.05}_{-0.05}$	60.4/82	$1.38^{+0.14}_{-0.20}$	$6.8^{+3.2}_{-2.7}$	$2.06^{+0.25}_{-0.18}$	15.3/25
z-golden (RF)	49	$0.86^{+0.14}_{-0.15}$	$5.3^{+1.2}_{-0.9}$	$1.71^{+0.05}_{-0.05}$	39.0/66	$1.02^{+0.19}_{-0.24}$	$4.6^{+1.6}_{-1.1}$	$1.83^{+0.09}_{-0.08}$	19.7/39
z-golden (OF)	49	$0.95^{+0.09}_{-0.11}$	$2.4^{+0.5}_{-0.4}$	$1.77^{+0.06}_{-0.05}$	40.1/40	$1.08^{+0.20}_{-0.24}$	$1.8^{+0.8}_{-0.4}$	$1.92^{+0.12}_{-0.11}$	14.7/17
15–50 keV ^a	244	$1.07^{+0.05}_{-0.05}$	$2.8^{+0.6}_{-0.5}$	$1.75^{+0.05}_{-0.04}$	58.8/46	$1.30^{+0.13}_{-0.14}$	$2.0^{+0.8}_{-0.5}$	$1.97^{+0.10}_{-0.09}$	11.2/15
50–150 keV ^a	244	$0.91^{+0.11}_{-0.14}$	$2.0^{+0.7}_{-0.5}$	$1.49^{+0.08}_{-0.07}$	14.0/24	$1.04^{+0.14}_{-0.18}$	$1.8^{+0.7}_{-0.5}$	$1.80^{+0.15}_{-0.12}$	6.3/14
$T_{90} > 80$ s ^a	90	$1.06^{+0.12}_{-0.07}$	$2.0^{+0.4}_{-0.3}$	$1.78^{+0.05}_{-0.06}$	31.3/32	$1.18^{+0.16}_{-0.18}$	$1.8^{+0.8}_{-0.4}$	$2.00^{+0.13}_{-0.12}$	8.6/13
$T_{90} < 40$ s ^a	90	$0.59^{+0.10}_{-0.11}$	$3.2^{+0.5}_{-0.4}$	$1.72^{+0.05}_{-0.04}$	93.6/59	$0.96^{+0.20}_{-0.25}$	$3.1^{+0.9}_{-0.5}$	$1.86^{+0.06}_{-0.06}$	22.1/37
$P < 0.4$ ^a	124	$1.03^{+0.07}_{-0.07}$	$2.1^{+0.4}_{-0.3}$	$1.73^{+0.06}_{-0.04}$	27.9/33	$1.25^{+0.14}_{-0.15}$	$1.8^{+0.5}_{-0.4}$	$2.03^{+0.11}_{-0.10}$	10.8/14
$P > 1.0$ ^a	65	$1.00^{+0.06}_{-0.06}$	$6.1^{+1.5}_{-1.0}$	$1.79^{+0.04}_{-0.04}$	109/115	$1.44^{+0.06}_{-0.09}$	$10.9^{+4.6}_{-3.4}$	$1.93^{+0.05}_{-0.06}$	89.5/117
$F < 4.4$ ^a	97	$0.80^{+0.10}_{-0.11}$	$3.0^{+1.0}_{-0.6}$	$1.65^{+0.05}_{-0.05}$	60.6/50	$0.94^{+0.16}_{-0.20}$	$2.0^{+0.6}_{-0.4}$	$1.79^{+0.08}_{-0.07}$	19.0/24
$F > 19.8$ ^a	30	$1.31^{+0.05}_{-0.04}$	$9.4^{+4.9}_{-1.1}$	$1.94^{+0.08}_{-0.04}$	120/106	$1.45^{+0.11}_{-0.14}$	$3.6^{+3.6}_{-0.9}$	$1.77^{+0.07}_{-0.07}$	19.4/44
$E_{\text{iso},52} < 9$ ^{b,c}	25	$1.04^{+0.10}_{-0.13}$	$6.2^{+2.5}_{-2.7}$	$1.70^{+0.09}_{-0.08}$	74.5/48	$1.21^{+0.07}_{-0.07}$	$8.6^{+2.2}_{-2.3}$	$2.14^{+0.23}_{-0.19}$	57.6/37
$E_{\text{iso},52} > 21$ ^{b,c}	25	$1.08^{+0.15}_{-0.17}$	$8.3^{+3.0}_{-2.0}$	$1.89^{+0.07}_{-0.07}$	73.5/81	–	–	$1.86^{+0.07}_{-0.07}$ ^d	31.1/43 ^d
$0.1 < z < 1.5$ ^b	32	$1.12^{+0.08}_{-0.08}$	$10.2^{+2.6}_{-2.2}$	$1.95^{+0.12}_{-0.11}$	50.6/48	–	–	$1.68^{+0.10}_{-0.11}$ ^d	18.2/14 ^d
$2.6 < z < 8.1$ ^b	32	$0.67^{+0.17}_{-0.22}$	$6.0^{+2.1}_{-1.3}$	$1.71^{+0.08}_{-0.07}$	45.0/54	–	–	$1.69^{+0.09}_{-0.10}$ ^d	17.6/28 ^d

Note: The average PDS of the samples denoted with ‘RF’ (‘OF’) refer to the source-rest frame (observer frame). The peak count rate p (count fluence F) is expressed in count s^{−1} det^{−1} (count det^{−1}) per fully illuminated detector for an equivalent on-axis source.

^aSelection from the full sample.

^bSelection from the z-silver sample.

^c $E_{\text{iso},52} = E_{\text{iso}}/10^{52}$ erg.

^dBest-fitting parameters refer to a simple power-law model.

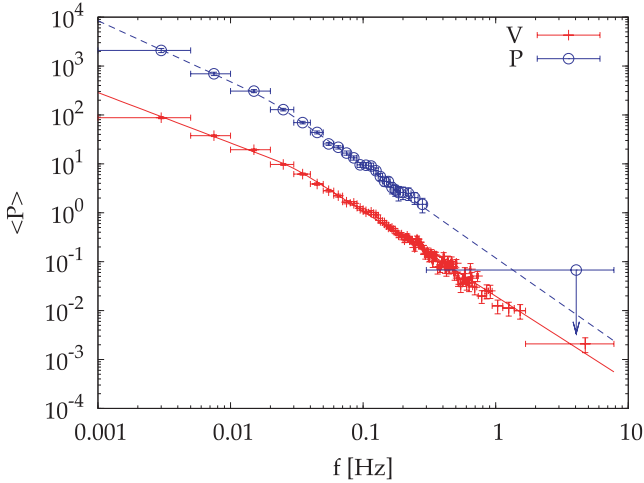


Figure 2. Average PDS for the full sample of 244 GRBs in the observer frame. The crosses (empty circles) correspond to the net variance (peak rate) normalization case. Upper limits are 2σ . The peak rate data have conveniently been shifted for the sake of clarity. The corresponding best-fitting broken power laws are also shown. Notably, the peak normalization has a poorer S/N due to the bright GRBs having a smaller weight than in the variance normalization; this becomes apparent at high frequencies, where the signal becomes comparable with statistical noise.

frame, f_b changes from 2.4×10^{-2} to 5.3×10^{-2} Hz. The ratio of 2.2 ± 0.6 between the source- and the observer-frame values of f_b is close to the average factor of $(1 + \hat{z}) \sim 3.2$, where $\hat{z} = 2.2$ is both median and mean redshift of the z-golden sample. Except for f_b , the comparison of the results obtained for the z-golden sample between

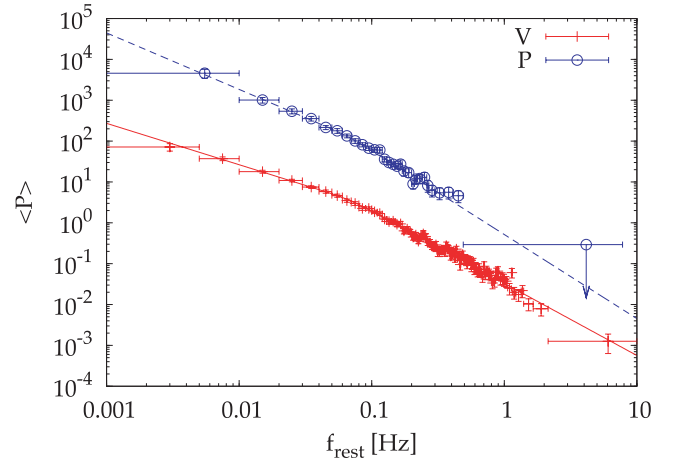


Figure 3. Average source-rest-frame PDS for the z-silver sample of 97 GRBs in the observed 15–150 keV energy band. Symbols are the same as in Fig. 2.

observer- and source-rest frame shows no significant differences in the power-law indices. The same conclusion holds when we compare the z-silver with the full sample. This result is not obvious: although power-law indices are clearly invariant observables, the impact of averaging out different source-frame energy bands on the observed PDS is not obvious.

Fig. 5 shows examples of light curves and their PDSs of individual GRBs randomly picked out from the full sample. While the global trend suggested by visual inspection favours the description of the average PDS with a power law with index compatible with ~ 1.7

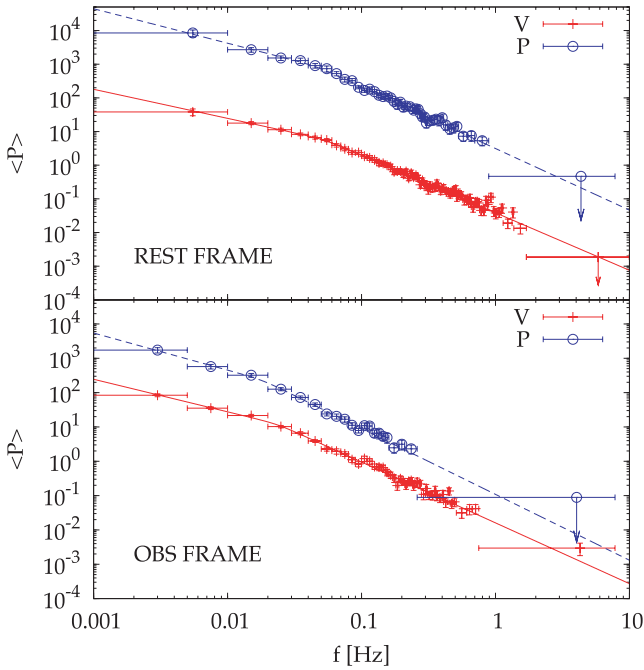


Figure 4. Top panel: average source-rest-frame PDS for the *z*-golden sample in the common 66–366 keV source-rest-frame energy band. Bottom panel: average PDS for the same sample in the 15–150 keV energy band (observer frame). Symbols are the same as in Fig. 2.

above a few 10^{-2} Hz, individual PDSs still exhibit a variety of different average declines.

3.1 Average PDSs at different energies

Remarkably different behaviours in the high-frequency power-law indices are observed for different observed energy bands: in the variance normalization, α_2 varies from $1.75^{+0.05}_{-0.04}$ to $1.49^{+0.08}_{-0.07}$ passing from 15–50 to 50–150 keV. The low-frequency index α_1 is also shallower at higher energies, $0.91^{+0.11}_{-0.14}$ to be compared with 1.07 ± 0.05 observed in the softer energy channel (Fig. 6).

The break frequency shows no significant dependence on energy. Analogous variations are observed in the peak normalizations, although the indices are systematically steeper, as noted above. The same trend was noted in the individual BATSE energy channels: the power-law index decreased from 1.72 in the 25–55 keV range to 1.50 above 320 keV (BSS00).

Fig. 7 directly compares our values with BSS00's as a function of energy. The BATSE data show a dependence on energy E which can be modelled with the power law $\alpha_2 \propto E^{-0.05}$. These results are compatible with ours within uncertainties (BSS00 do not provide uncertainties on their values). Curiously, the variance normalization, which is preferable to us also for the reasons explained below in Section 3.7, is in better agreement with BSS00 results than the peak normalization, which BSS00 adopted for their analysis.

3.2 The effects of GRB durations

The cut-off frequency f_b is mainly connected with the average duration of the GRBs and of the individual pulses they consist of, as noted above when moving from the observer to the source-rest frame. We investigated the role of the duration by selecting two subsets of the full sample with extreme durations, each collecting 90 GRBs.

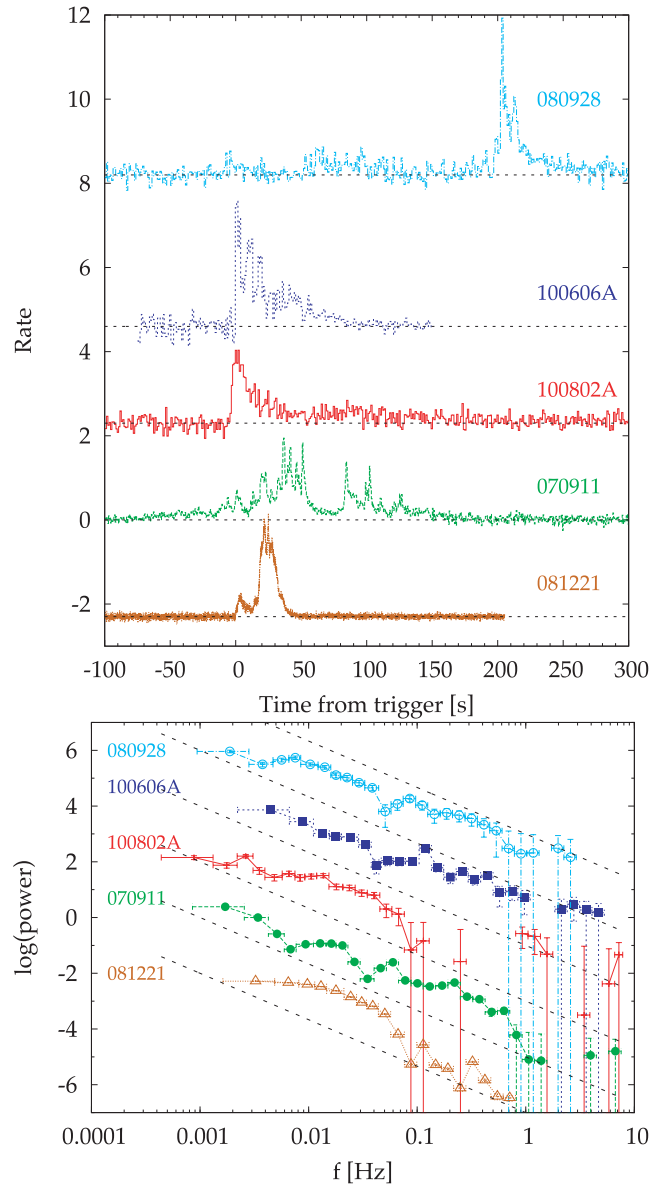


Figure 5. Top panel: examples of light curves of individual GRBs randomly selected from the full sample. Data are shifted along the y-axis for clarity. Bottom panel: the corresponding PDSs. The dashed lines are power laws with index 5/3.

In principle, because of the finiteness of the GRB duration, and therefore of the temporal window which contains its time profile, the observed PDS is the convolution of the true one with $|\sin(f\pi T)/(f\pi)|^2$, where f is the frequency and T is the length of the window (e.g. van der Klis 1989). In practice, all the features in the true PDS narrower than $1/T$ are smoothed out, and the minimum frequency that can be explored, $1/T$, also defines the resolution of the PDS. Provided that $T \gg \tau$, where τ is a generic characteristic time-scale acting in a GRB, the cut-off frequency associated with it, $\approx 1/\tau$, is unaffected.

Fig. 8 shows the duration distributions for the full sample as well as for the two subsets chosen by us: GRBs with $T_{90} < 40$ and $T_{90} > 80$ s on the other side. The top panel of Fig. 9 displays the average PDS of both subsamples. The logarithmic average durations of each subsample are 15 and 153 s, respectively. Indeed, f_b decreases from 3.2×10^{-2} of the shortest GRBs to 2.0×10^{-2} Hz of the longest ones

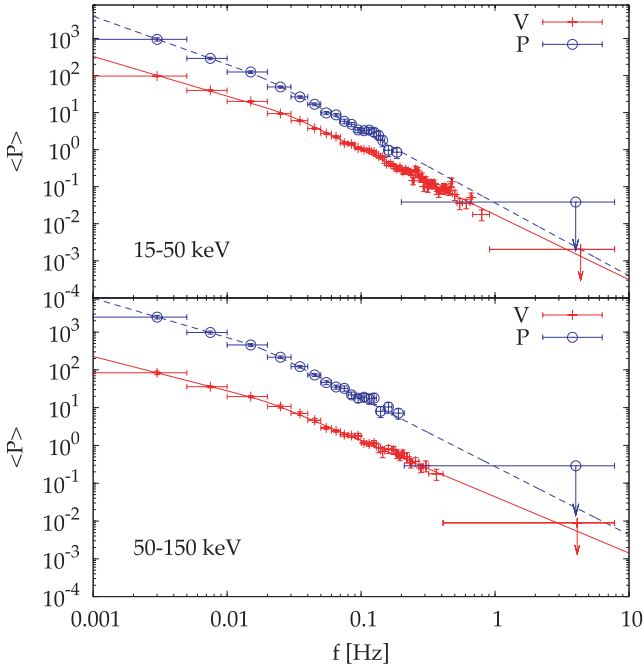


Figure 6. Top panel: average PDS for the full sample in the 15–50 keV energy band (observer frame). Bottom panel: average PDS for the same sample in the 50–150 keV energy band. Symbols are the same as in Fig. 2.

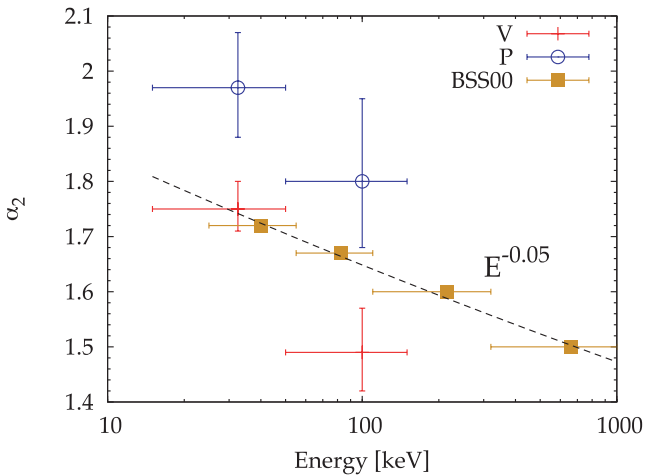


Figure 7. High-frequency power-law index α_2 as a function of energy E obtained by fitting the average PDS of the full sample within the variance (crosses) and the peak (circles) normalizations. BSS00 results derived from BATSE GRBs are also shown (squares). The dashed line shows the power law $\alpha_2 \propto E^{-0.05}$.

(Table 4). The change of f_b is not comparable to the corresponding change in the average duration. However, the low-frequency power-law index α_1 significantly steepens from ~ 0.6 to ~ 1.1 in the variance normalization. This suggests that different values of f_b may affect the estimate of α_1 , because the asymptotic behaviour is not reached when f_b is close to the lowest explorable frequency, and is more affected by the finite width at low frequencies. Moreover, the cut-off frequency is more sensitive to the average characteristic times (both rise and decay times) of individual shots, rather than to the overall duration: e.g. the PDS of a simple exponential shot with a characteristic time τ has $f_b \sim 1/2\pi\tau$ (e.g. Lazzati 2002). This

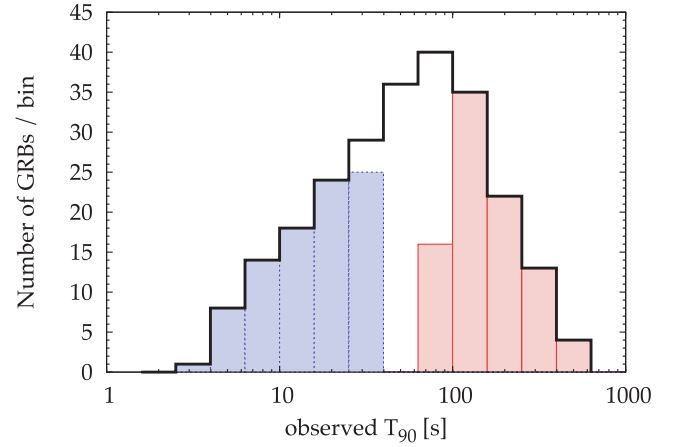


Figure 8. T_{90} distribution for the full sample (solid line). The shaded histograms show two subsets including 90 GRBs each with the shortest and longest durations, respectively.

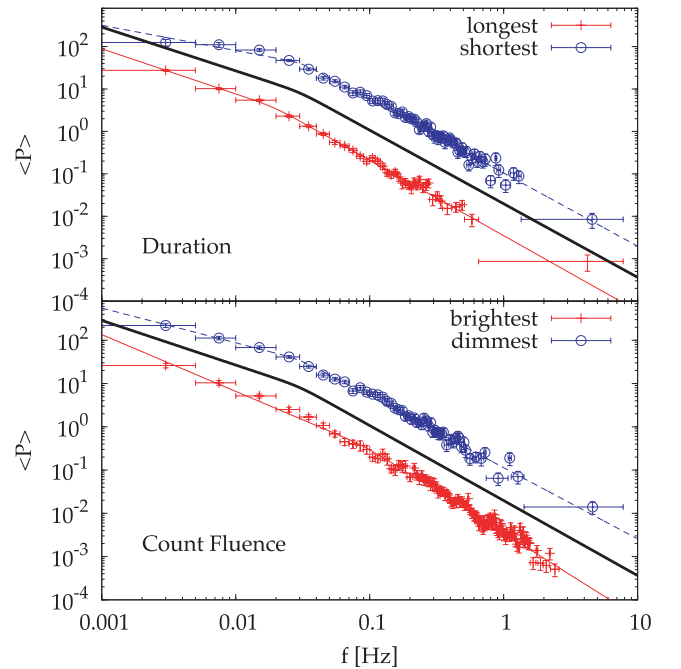


Figure 9. Top panel: average PDS for two subsets with extreme durations: 90 shortest versus 90 longest duration GRBs. Bottom panel: average PDS for two subsets with extreme count fluences: 30 highest fluence versus 97 lowest fluence GRBs. The thick solid lines are the best fit for the full sample. Different data sets are shifted for clarity reasons.

is still true in the presence of shot noise (Frontera & Fuligni 1979; Belli 1992), provided that the occurrence times of the shots are independently distributed. Although this is a rough approximation in this case, the best-fitting values of f_b imply characteristic times of individual shots about 5–8 s (2–4 s) long in the observer (source rest) frame.

3.3 The effects of GRB peak rates and fluences

Similarly, we investigated the effects of both the peak count rate and fluence on the average PDS by selecting proper subsets of the full sample. Unlike for the duration, the S/N does depend on both peak rate and fluence. We ensured comparable statistical quality of

the two subsets by collecting more faint bursts (both in terms of peak rates and count fluence). As for the peak rate p , we ended up with 124 and 65 GRBs with $p < 0.4$ and $p > 1.0$ count s⁻¹ det⁻¹, respectively. The fluence F -selected subsets include 97 and 30 bursts with $F < 4.4$ and $F > 19.8$ count det⁻¹, respectively. Both peak rate and count fluence distributions are shown in the projected histograms of Fig. 1.

Concerning the peak rate, the best-fitting power-law indices are the same for both subsamples. Instead, f_b increases by a factor of 3 (5) in the variance (peak) normalization when we move from the faint to the bright subset. This is due to the brighter pulses being narrower (Norris et al. 1996): on average the GRBs of our faint subset have three to five times longer pulses than those of the bright subset. This seems to be at variance with the results by BSS00, who found a decreasing power-law index with increasing peak count rate: from 1.82 for the faintest GRBs down to 1.63 for the brightest end.

Concerning α_1 , only for the count fluence sample this index becomes shallower when moving from the high- to low-fluence subset. The same behaviour is observed for the duration-driven subsamples (Section 3.2) when we move from the longest to the shortest GRBs. This common property is explained by the shortest GRBs having lower fluence on average, as confirmed by the correlation between fluence and T_{90} for both the full and the z -silver samples with significance values of the order of 10^{-11} and 0.1–0.2 per cent, respectively, according to the non-parametric tests of Spearman and Kendall.

We note that the estimate of the power-law index within a given range can be affected by the choice of the model: from fig. 8 of BSS00, the range over which the power law is fitted extends over a single decade. Within such a limited range the fitted slope is sensitive to the frequency interval chosen for modelling. Within our data, when we opt for a smoother break in equation (1) by fixing $n = 1$, the best-fitting values for the post-break frequency slope α_2 are systematically steeper, because the asymptotic value is not reached within the range covered by the data (Section 3.6).

In equation (1) this may introduce an artificial correlation between f_b and α_2 (as well as α_1): the higher f_b , the steeper α_2 , when the frequency range covered by the data is not sufficiently broad. Indeed, we observe this in the fluence-driven subsets, as reported in Table 4 and shown in the bottom panel of Fig. 9. Only in the variance normalization case, α_2 varies from 1.65 (faint subset) to 1.94 (bright subset), whereas f_b increases by a factor of 3.1. No such change is observed in the peak normalization case, where both f_b and α_2 experience very little changes.

We checked whether the results obtained on the fluence-driven subsets are affected by the corresponding average S/N. We split the sample into two subsets of 50 and 150 GRBs having the highest and lowest S/N PDSs, respectively. Within uncertainties the two average PDSs showed no distinctive behaviour. Therefore, the variety of S/N is not directly responsible for the different PDS properties of fluence-driven subsets.

3.4 The effects of different E_{iso} and $L_{\text{p,iso}}$

Here we investigate the possible existence of correlations between the PDS and intrinsic properties of the prompt emission. Out of the z -silver sample, we selected the GRBs with measured intrinsic peak energy of the time-averaged $E F(E)$ spectrum, the so-called $E_{\text{p,i}}$. The isotropic-equivalent gamma-ray released energy in the 1–10⁴ keV band, E_{iso} , which correlates with $E_{\text{p,i}}$ (Amati et al. 2002), is also known for the same events. We adopted the standard cosmological model: $H_0 = 71$ km s⁻¹ Mpc⁻¹, $\Omega_\Lambda = 0.73$, $\Omega_M = 0.27$ (Spergel

et al. 2003). The values for both $E_{\text{p,i}}$ and E_{iso} are taken from Amati et al. (2008), Amati et al. (in preparation) and Amati, Frontera & Guidorzi (2009). We ended up with a subset of 64 GRBs. For the same bursts we estimated the isotropic-equivalent peak luminosity, $L_{\text{p,iso}}$, by normalizing E_{iso} through the ratio between peak count rate and count fluence in the source-rest frame. This implicitly assumes no spectral evolution throughout the prompt emission, which for instance does not hold when the hardness ratio tracks the time profile. This leads to underestimating the peak luminosity by a factor of a few in the worst case. However, in a logarithmic space this cannot wash out possible genuine correlations or build fake ones, but it may merely increase the observed dispersion. The values of E_{iso} , $E_{\text{p,i}}$ and $L_{\text{p,iso}}$ for this subsample are reported in Table 5.

We compared the average PDS of the least and that of the most energetic GRBs as follows: we collected two subsets of 25 GRBs each, with extreme values of E_{iso} . Each subset collects about 1/3 of the overall set. The least energetic GRBs all have $E_{\text{iso}} < 9 \times 10^{52}$ erg, while the most energetic ones all have $E_{\text{iso}} > 2.1 \times 10^{53}$ erg, with logarithmic average values of 2.8×10^{52} and 4.7×10^{53} erg, respectively. The average PDSs of the two groups are not found to significantly differ from one another, as reported in Table 4.

Analogously, we divided the same sample according to different classes of $L_{\text{p,iso}}$, and in none of the cases we found evidence for a dependence of the average PDS on $L_{\text{p,iso}}$.

3.5 The effects of redshift

We considered two classes of 32 GRBs each with the lowest and highest redshift values, respectively, among the z -silver sample. The aim is to study possible evolutionary effects. The choice of the number of GRBs is a trade-off between the need for a big enough sample for statistical purposes and the need of having two well-separated redshift bins. We came up with two classes: the low- z GRBs with $0.1 < z < 1.5$ and the high- z ones with $2.6 < z < 8.1$. The mean (median) redshifts for both subsets are 0.9 (0.9) and 3.5 (3.2), respectively. The corresponding average PDSs are shown in Fig. 10 together with their best-fitting models (Table 4). Similarly to what is observed for the low-fluence GRBs, for the variance normalization the average PDS of high- z GRBs has shallower indices: α_1 and α_2 are, respectively, $0.67^{+0.17}_{-0.22}$ and $1.71^{+0.08}_{-0.07}$, to be compared with 1.12 ± 0.08 and $1.95^{+0.12}_{-0.11}$ found for the low- z GRBs. To understand whether this is due to the farther GRBs having lower fluence values on average, in Fig. 11 we studied the correlation between fluence and redshift for the full z -silver sample as well as for the two subsets considered here. There is a hint for an anticorrelation between observed fluence and redshift, whose significance is about 0.2–0.3 per cent according to non-parametric tests (Spearman and Kendall). The fluence distributions of the low- and of the high- z subsets have a K–S probability of 1.6 per cent of being drawn from the same population. As for the fluence, the z -silver sample is an unbiased subset of the full sample, since the two fluence distributions are fully compatible (46 per cent probability according to a K–S test). Thus, the low-fluence subset of the full sample discussed in Section 3.3 is likely to include more high- z bursts than what the high-fluence subset does. On average, the high-fluence bursts have lower redshifts and this explains the common properties observed in the average PDS, compared with that of low-fluence and high-redshift GRBs. Given the correlation between fluence and T_{90} , we checked whether for the z -silver sample the redshift also correlates with the observed T_{90} and we found it does not. Therefore, while the fluence correlates with T_{90} and anticorrelates with redshift, the latter does not correlate with T_{90} .

Table 5. The subsample of 64 GRBs with measured $E_{p,i}$, E_{iso} and $L_{p,iso}$.

GRB	z	$\text{Log}(E_{iso,52})^a$	$\text{Log}(E_{p,i})^b$	$\text{Log}(L_{p,iso,51})^c$
050318	1.440	0.361 ± 0.031	2.050 ± 0.096	1.036 ± 0.041
050401	2.900	1.566 ± 0.086	2.657 ± 0.104	2.211 ± 0.093
050525A	0.606	0.402 ± 0.076	2.117 ± 0.013	1.031 ± 0.076
050603	2.821	1.806 ± 0.031	3.123 ± 0.035	3.103 ± 0.040
050820A	2.612	2.013 ± 0.035	3.113 ± 0.092	2.271 ± 0.044
060115	3.530	0.822 ± 0.066	2.452 ± 0.052	0.907 ± 0.074
060206	4.048	0.653 ± 0.097	2.593 ± 0.051	1.725 ± 0.099
060418	1.489	1.123 ± 0.088	2.743 ± 0.111	1.387 ± 0.092
060526	3.210	0.436 ± 0.058	2.012 ± 0.088	0.951 ± 0.080
060607A	3.080	1.065 ± 0.102	2.666 ± 0.109	1.253 ± 0.104
060614	0.125	-0.702 ± 0.184	1.500 ± 0.500	-0.841 ± 0.187
060707	3.425	0.755 ± 0.084	2.443 ± 0.044	0.978 ± 0.097
060814	0.840	0.856 ± 0.043	2.650 ± 0.148	0.702 ± 0.045
060908	1.884	1.013 ± 0.042	2.702 ± 0.087	1.522 ± 0.052
060927	5.600	1.166 ± 0.063	2.675 ± 0.043	2.198 ± 0.069
061007	1.261	1.952 ± 0.044	2.945 ± 0.061	1.859 ± 0.046
061121	1.314	1.368 ± 0.050	3.107 ± 0.052	1.867 ± 0.051
061126	1.159	1.494 ± 0.050	3.105 ± 0.138	1.961 ± 0.053
061222A	2.088	1.468 ± 0.094	2.935 ± 0.075	2.004 ± 0.095
071003	1.604	1.580 ± 0.052	3.313 ± 0.060	1.805 ± 0.058
071010B	0.947	0.189 ± 0.239	1.996 ± 0.087	0.493 ± 0.239
071020	2.145	0.951 ± 0.213	3.000 ± 0.069	2.026 ± 0.214
071117	1.331	0.614 ± 0.104	2.783 ± 0.158	1.608 ± 0.106
080319B	0.937	2.070 ± 0.033	3.100 ± 0.022	1.901 ± 0.034
080319C	1.950	1.164 ± 0.089	2.937 ± 0.135	1.830 ± 0.094
080411	1.030	1.209 ± 0.026	2.715 ± 0.058	1.613 ± 0.027
080413A	2.433	0.920 ± 0.108	2.745 ± 0.138	1.546 ± 0.109
080413B	1.100	0.397 ± 0.047	2.167 ± 0.088	1.359 ± 0.053
080603B	2.690	1.062 ± 0.012	2.559 ± 0.118	1.684 ± 0.029
080605	1.640	1.403 ± 0.031	2.811 ± 0.037	1.965 ± 0.035
080607	3.036	2.300 ± 0.024	3.224 ± 0.058	2.898 ± 0.032
080721	2.591	2.119 ± 0.075	3.237 ± 0.057	2.886 ± 0.086
080810	3.350	1.676 ± 0.050	3.164 ± 0.053	1.874 ± 0.063
080916A	0.689	0.025 ± 0.036	2.263 ± 0.043	-0.053 ± 0.041
080928	1.692	0.589 ± 0.100	1.965 ± 0.107	0.833 ± 0.108
081008	1.968	0.998 ± 0.040	2.408 ± 0.088	0.795 ± 0.049
081028	3.038	1.261 ± 0.044	2.332 ± 0.183	0.736 ± 0.053
081222	2.770	1.503 ± 0.050	2.702 ± 0.029	2.172 ± 0.051
090102	1.547	1.351 ± 0.052	3.056 ± 0.063	1.767 ± 0.073
090418A	1.608	1.230 ± 0.069	3.182 ± 0.109	1.200 ± 0.078
090423	8.100	1.060 ± 0.138	2.652 ± 0.188	2.234 ± 0.142
090424	0.544	0.660 ± 0.091	2.436 ± 0.008	1.284 ± 0.092
090516	4.109	1.848 ± 0.085	2.949 ± 0.185	1.843 ± 0.107
090618	0.540	1.340 ± 0.052	2.404 ± 0.070	0.943 ± 0.052
090715B	3.000	1.372 ± 0.067	2.706 ± 0.144	1.666 ± 0.069
090812	2.452	1.670 ± 0.076	3.273 ± 0.159	1.997 ± 0.081
090926B	1.240	0.555 ± 0.022	2.309 ± 0.021	0.394 ± 0.032
091018	0.971	-0.097 ± 0.044	1.710 ± 0.165	0.788 ± 0.046
091020	1.710	0.957 ± 0.134	2.313 ± 0.359	0.298 ± 0.136
091024	1.092	1.743 ± 0.042	2.724 ± 0.199	1.499 ± 0.052
091029	2.752	0.947 ± 0.040	2.343 ± 0.128	1.180 ± 0.045
091127	0.490	0.172 ± 0.051	1.731 ± 0.040	0.986 ± 0.058
091208B	1.063	0.398 ± 0.031	2.404 ± 0.043	1.396 ± 0.052
100621A	0.542	0.447 ± 0.055	2.159 ± 0.069	0.258 ± 0.056
100814A	1.440	1.183 ± 0.051	2.410 ± 0.057	0.909 ± 0.053
100906A	1.727	1.474 ± 0.040	2.455 ± 0.070	1.718 ± 0.043
101213A	0.414	0.426 ± 0.085	2.604 ± 0.189	0.102 ± 0.093
110205A	2.220	1.680 ± 0.058	2.841 ± 0.185	1.436 ± 0.063
110213A	1.460	0.757 ± 0.061	2.325 ± 0.149	1.259 ± 0.072
110422A	1.770	1.900 ± 0.045	2.622 ± 0.043	2.164 ± 0.046
110503A	1.613	1.317 ± 0.038	2.739 ± 0.047	2.163 ± 0.043
110715A	0.820	0.637 ± 0.044	2.341 ± 0.040	1.504 ± 0.045
110731A	2.830	1.692 ± 0.040	3.065 ± 0.022	2.576 ± 0.042
110818A	3.360	1.423 ± 0.045	3.037 ± 0.095	1.526 ± 0.067

^a $E_{iso,52} = E_{iso}/10^{52}$ erg.^b $E_{p,i}$ is expressed in keV and is measured in the source-rest frame.^c $L_{p,iso,51} = L_{p,iso}/10^{51}$ erg s⁻¹.

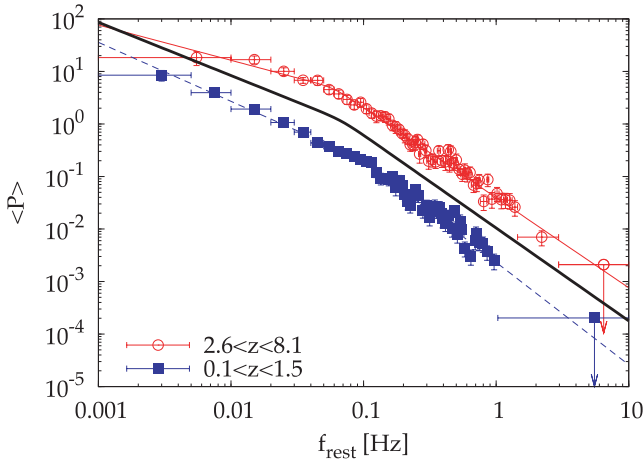


Figure 10. Average source-rest-frame PDS for two subsets with different redshift bins taken from the z -silver sample: low- z (filled squares), and high- z (empty circles), together with their corresponding best-fitting models. For comparison, the thick solid line shows the best-fitting model obtained over the entire z -silver sample.

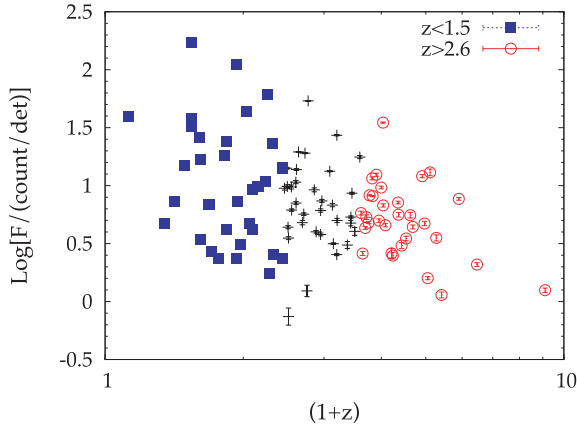


Figure 11. Count fluence versus redshift z distribution for the z -silver sample. The two subsets with different redshift bins are also shown with the same symbols as in Fig. 10.

Qualitatively, the shallower power-law indices for the low-fluence/high- z GRBs can be explained by the result found on the average PDSs of different energy channels (Section 3.1 and Fig. 7): harder photons have a shallower PDS (see also Table 4). Given that the light curves of the z -silver sample refer to the common *observed* 15–150 keV energy band, the results obtained for the high- z subset refer to a harder source-rest-frame energy band. Whether this difference between the average PDS of low- and that of high- z GRBs can entirely be ascribed to the cosmological shift of the energy band, or it is due to an evolutionary property of GRBs is not clear. To clarify this issue, we should apply the same analysis to the z -golden sample: however, practically this is not feasible due to the low number of GRBs, the limited range both in z (Section 2.2) and in fluence (Fig. 1).

3.6 Smoothness of the break

In Section 3.3 we noted that choosing a smoother break in equation (1), e.g., $n = 1$ instead of $n = 10$, yields systematically shallower (steeper) values for α_1 (α_2). The differences in α_2 between $n = 10$ and $n = 1$ are however milder and in all cases they are compatible

with zero within uncertainties. Analogously, f_b is systematically lower for a smoother break, although not significantly. Overall, allowing the data to be fitted with a smoother break implies that the asymptotic regime at low frequencies is not covered by the data, and this leads to shallower values for α_1 than what data actually exhibit. The goodness of the fits in both cases is similar and shows no systematic behaviour.

We conclude that the degree of freedom brought in by the smoothness of the break of equation (1) does not affect significantly the estimates of α_2 , thanks to the broader frequency range at $f > f_b$ covered by the data.

3.7 PDS distribution

PDSs of individual GRBs are very different from each other (Fig. 5). For instance, let us consider a single fast-rise exponential decay with a characteristic time τ (either rise or decay time). At $f \gg 1/\tau$ the PDS asymptotically declines as a power law with an index of 2 or steeper. Depending on the peakedness value, the PDS can also exhibit oscillatory terms in the decay, as shown by Lazzati (2002). Oscillations modulating the power-law decline can also appear in the PDS of those GRBs with two or more pulses separated by a quiescent time, which makes them interfere in the Fourier transform (since the PDS can also be seen as the Fourier transform of the autocorrelation function, as stated by the Wiener–Khinchin theorem).

When for each frequency bin we average out the power for a given set of GRBs, we implicitly assume that each time profile is an individual realization of a common stochastic process. On the contrary, if one is interested in studying the light curve of a single GRB, and treats it like a deterministic signal affected by uncorrelated noise, the averaging process does not make sense any more (e.g. Guidorzi 2011).

Under the assumption of a unique stochastic process explaining the variety of observed GRB light curves, we study the power distribution as a function of frequency. BSS98 found that for peak normalization for a given frequency bin f_j , the fluctuations $P_i(f_j)$ around the average power $\bar{P}(f_j)$ (i running over a given set of GRBs) are minimal and the distribution is an exponential, $dN/dP(f_j) = N \exp[-P(f_j)/\bar{P}(f_j)]$. For each grouped frequency bin we investigated the observed distribution. For both normalizations we did not subtract the Poisson noise. Fig. 12 displays four distributions corresponding to four different frequency bins for the full sample of GRBs in the variance normalization. We adopted the Anderson–Darling test (Anderson & Darling 1952) implemented under the *R* package *ADGOFTEST*⁴ (v0.1) to test the compatibility with an exponential. This test is particularly sensitive to the distribution tails and, as such, to the possible presence of a few outliers. The corresponding probability was evaluated as a function of frequency for both normalizations and for different GRB sets. The results are shown in the top panels of Fig. 13. We also studied the ratio between the standard deviation of the observed distribution and that expected in the exponential distribution hypothesis (bottom panels of Fig. 13).

For all the GRB sets the fluctuations of the variance normalization are systematically lower than in the peak normalization. In the full sample case (top panel of Fig. 13), at low frequencies the P -value of the variance normalization is $\approx 10^{-5}$, due to the small dispersion of the distribution compared to that expected for an exponential.

⁴ <http://cran.r-project.org/web/packages/ADGofTest/>

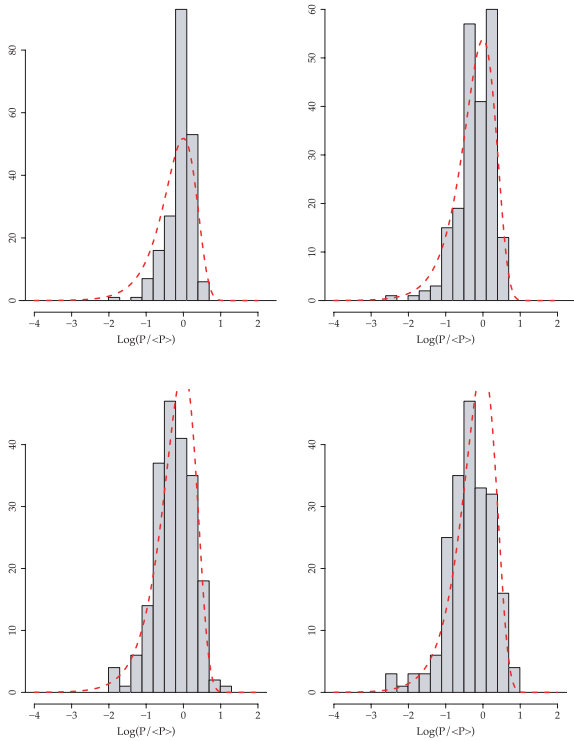


Figure 12. Observed distributions of the power at four different frequency bins from the full sample: from top to bottom, left to right, 0.01–0.02, 0.05–0.06, 0.23–0.24 and 0.40–0.41 Hz, respectively. The dashed lines show the corresponding expected exponential distribution, $dN/dP \propto \exp(-P/\bar{P})$.

At $f \gtrsim$ a few 10^{-2} Hz the P -value rises above 0.01 and finally decreases again below 0.01 at $f >$ a few 0.1 Hz. For less numerous sets, such as the z -silver and golden samples (mid- and bottom panels of Fig. 13, respectively), the exponential hypothesis cannot be rejected at almost any frequency for the variance normalization. For the peak normalization, the high-frequency range ($f \gtrsim 1$ Hz) exhibits systematically worse P -values and larger fluctuations around the average power.

In conclusion, the variance normalization shows minimal fluctuations around the average power and the PDS is distributed most consistently with an exponential. This is also a χ^2 distribution with two degrees of freedom (χ^2_2) and suggests that the properly normalized power of each GRB at any given frequency is the result of a Fourier transform term, whose amplitude is normally distributed around the average value and the phase is independently and uniformly distributed (van der Klis 1989). The fluctuations around the mean value become significantly larger than what were expected for a χ^2_2 distribution above ~ 1 Hz in the largest samples (Fig. 13). In our data at these frequencies the statistical noise becomes comparable with signal, and this could be connected with it, although the details are not clear. Alternatively, it could be suggestive of the presence of a fraction of GRBs with significantly more power at high frequencies than the bulk of GRBs.

Concerning the relative weight of some GRBs in driving the average results, none of the classes considered above (Sections 3.2, 3.3 and 3.4) seems to be dominant in determining the observed properties, especially the high-frequency slope α_2 . By definition, the variance normalization equally weighs each GRB in the average (noise-subtracted) PDS, since the normalized PDSs of both bright and dim GRBs have the same area. The only difference is that dim GRBs have a lower S/N, and, as a consequence, they can

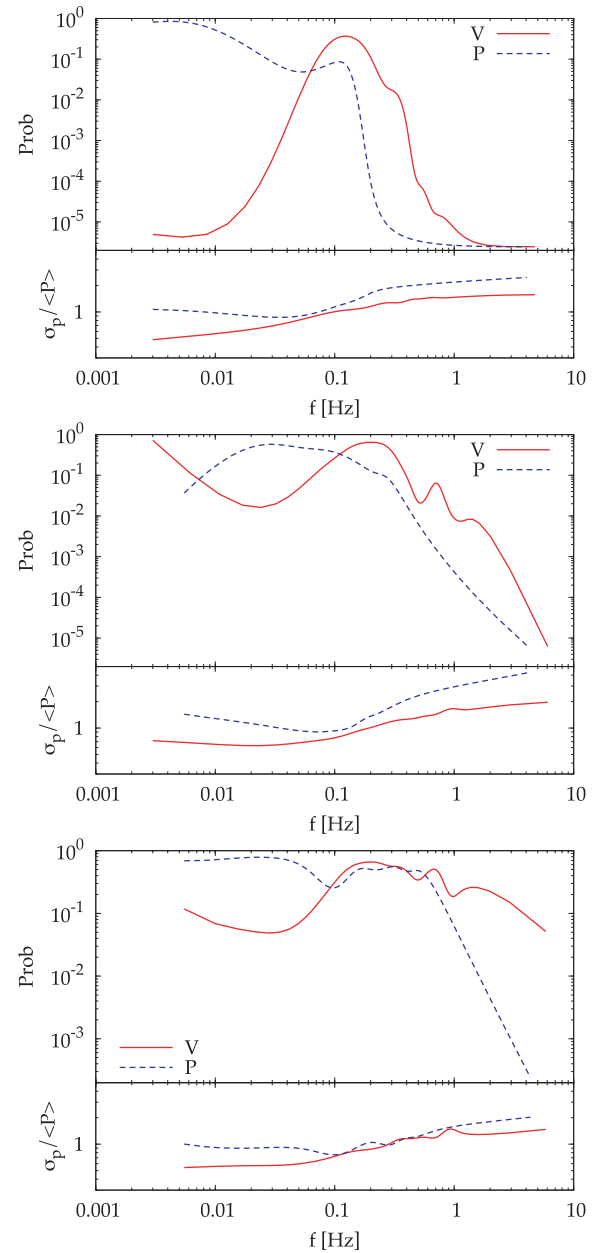


Figure 13. Top panel: P -value based on the Anderson–Darling test that the corresponding density distribution of power as a function of frequency is consistent with an exponential. The ratio between the σ of the observed power distribution over the corresponding average value is also shown. The solid (dashed) line shows the variance (peak) normalization case. GRBs are from the full sample. Mid-panel: the same, with GRBs being taken from the z -silver sample. Bottom panel: the same, with GRBs from the z -golden sample.

contribute more than bright GRBs to the observed scatter in the power distribution.

4 CONCLUSIONS

For the first time it was possible to study the average PDS of a sample of long GRBs by correcting for the cosmological time dilation effects both on timing and spectral properties. This is described by a smoothed broken power law, with a typical low- (high-) frequency index around 1.0 (1.7–1.8), and a break frequency of a

few $\times 10^{-2}$ Hz. This is mainly determined by an average rest-frame characteristic time of 2–4 s for the individual shot most GRBs are made of. We found no clear difference from what is obtained by processing the same sample within the observer frame, apart from the break frequency f_b . In particular, for a restricted sample of 64 GRBs with known E_{iso} , $L_{\text{p,iso}}$ we found no correlation between intrinsic properties and the average rest-frame PDS.

Comparing different energy bands, in agreement with previous results we found that the average PDS in the harder energy channel exhibits shallower indices, especially at high frequencies. From the sample of GRBs with known redshift, we found that in the observed 15–150 keV energy band the average PDS of the high- z GRBs, which also have lower fluences on average, exhibits marginally shallower indices than the average PDS of the low- z /higher fluence GRBs. In principle, this can be explained by the farthest GRBs being observed in source-rest-frame harder energy bands. Whether this property is entirely due to the cosmological energy band shift bias, or it implies some evolution in the average PDS with redshift, cannot be settled with the present data set, because of the narrow passband of BAT.

In the observer frame the shortest GRBs ($3 < T_{90} < 40$ s), which on average have lower fluences as well, are characterized by higher values of f_b and shallower values of the low-frequency power-law index. This suggests that, within the covered frequency range, they better approach the asymptotic value of a flat PDS at low frequencies.

In most cases the high-frequency index for different GRB samples is compatible with 5/3 expected for a Kolmogorov velocity spectrum in a turbulent medium, but in fewer cases it can also be as steep as ~ 2 with no break in the power law up to several Hz.

At variance with past results, we do not find evidence for any cut-off around 1–2 Hz in the average PDS. Instead, for the full and the z -silver samples the average PDS is consistent with an unbroken power law up to several Hz at the least (Figs 2 and 3). However, the softer energy band of BAT compared with that of BATSE might account for the missing cut-off above 1 Hz.

Theoretical interpretations of the power-law PDS with an index compatible with 5/3 have been proposed in several different contexts. Within the internal shock model, by tuning the flow of mass and energy emission through the wind of shells it is possible to obtain the average power law in the PDS (Panaitescu et al. 1999; Spada et al. 2000). The observed PDS index is also obtained from emission due to a relativistic outflow of a jet propagating through the stellar and the circumstellar matter (Zhang, MacFadyen & Wang 2009; Morsony, Lazzati & Begelman 2010).

Alternatively to the classical internal shock model in which the energy of the ejecta is mostly kinetic, in the magnetically dominated outflows the energy dissipation via magnetic reconnection plays a crucial role (e.g. Lyutikov 2006; Zhang & Yan 2011, and references therein). In the ICMART model, the rapid reconfiguration of the magnetic field can trigger magnetohydrodynamic (MHD) turbulence, which ends up in a runaway release of synchrotron gamma-rays radiated by the accelerated particles. Unlike the hydrodynamical turbulence characterized by the 5/3 Kolmogorov velocity spectrum, MHD turbulence scales differently for different directions with respect to the field lines: the index ranges from 5/3 to 2 moving from perpendicular to parallel direction (Zhang & Yan 2011). Interestingly, this range matches our results.

Within some models, the observed variability may track that of the progenitor, e.g., through erratic accretion episodes (e.g. Kumar, Narayan & Johnson 2008), or hydrodynamical or magnetic instabilities in the accretion disc (e.g. Perna, Armitage & Zhang 2006; Proga

& Zhang 2006; Margutti et al. 2011). In particular, variability can also arise from turbulence within the accretion disc. For instance, in the context of magneto-rotational instability, Carballido & Lee (2011) studied how neutrino cooling can shape different PDSs of the observed luminosity, depending on the cooling process. Neutrino emissivity scales with temperature T as $\dot{q} \propto T^\beta$, where β is 9 (6) when e^\pm pair annihilation (e^\pm capture by free neutrons or protons) is the dominant process. They found that the range of power-law indices expected in the average PDS from 0.1 to 100 Hz varies between 1.7 and 2.0 with no clear break around 1–2 Hz, and with some bumps above 1–10 Hz which flatten the decline. Most of our values for the high-frequency power-law index are closer to 1.7 (Table 4), and according to the neutrino-cooling interpretation, on average this would favour larger values for β , i.e. where pair annihilation is dominant. However, due to S/N limitations, our present data set do not allow us to explore the average properties at high (> 10 Hz) frequencies, and the GRBs with sufficient signal are too few to draw statistically sound conclusions. Hopefully, in the future more numerous samples of GRBs with high S/N especially at high (> 10 Hz) frequencies will allow us to better discriminate between competing models.

ACKNOWLEDGMENT

CG acknowledges ASI for financial support (ASI-INAF contract I/088/06/0).

REFERENCES

- Amati L. et al., 2002, *A&A*, 390, 81
- Amati L., Guidorzi C., Frontera F., Della Valle M., Finelli F., Landi R., Montanari E., 2008, *MNRAS*, 391, 577
- Amati L., Frontera F., Guidorzi C., 2009, *A&A*, 508, 173
- Anderson T. W., Darling D. A., 1952, *Ann. Math. Statistics*, 23, 193
- Barthelmy S. D. et al., 2005, *Space Sci. Rev.*, 120, 143
- Belli B. M., 1992, *ApJ*, 393, 266
- Beloborodov A. M., Stern B. E., Svensson R., 1998, *ApJ*, 508, L25 (BSS98)
- Beloborodov A. M., Stern B. E., Svensson R., 2000, *ApJ*, 535, 158 (BSS00)
- Bhat P. N., Fishman G. J., Meegan C. A., Wilson R. B., Brock M. N., Paciesas W. S., 1992, *Nat*, 359, 217
- Carballido A., Lee W. H., 2011, *ApJ*, 727, L41
- Cenko S. B. et al., 2010, *AJ*, 140, 224
- De Luca A., Esposito P., Israel G. L., Götz D., Novara G., Tiengo A., Mereghetti S., 2010, *MNRAS*, 402, 1870
- Fenimore E. E., in 't Zand J. J. M., Norris J. P., Bonnell J. T., Nemiroff R. J., 1995, *ApJ*, 448, L101
- Frontera F., Fuligni F., 1979, *ApJ*, 232, 590
- Galassi M., Davies J., Theiler J., Gough B., Jungman G., Alken P., Booth M., Rossi F., 2009, *GNU Scientific Library Reference Manual*, 3rd edn., Network Theory Ltd., United Kingdom, ISBN 0954612078
- Gao H., Zhang B.-B., Zhang B., 2011, *ApJ*, preprint (arXiv:1103.0074)
- Gehrels N. et al., 2004, *ApJ*, 611, 1005
- Ghisellini G., 2011, in Romero G. E., Sunyaev R. A., Belloni T., eds, *Proc. IAU Symp. 275, Jets at all Scales*. Cambridge Univ. Press, Cambridge, p. 335
- Guidorzi C., 2011, *MNRAS*, 415, 3561
- Israel G. L., Stella L., 1996, *ApJ*, 468, 369
- Kawanaka N., Kohri K., 2011, *MNRAS*, 419, 713
- Kumar P., Narayan R., Johnson J. L., 2008, *MNRAS*, 388, 1729
- Lazzati D., 2002, *MNRAS*, 337, 1426
- Leahy D. A., Darbro W., Elsner R. F., Weisskopf M. C., Sutherland P. G., Kahn S., Grindlay J. E., 1983, *ApJ*, 266, 160 (L83)
- Lyutikov M., 2006, *New J. Phys.*, 8, 119
- MacFadyen A. I., Woosley S. E., 1999, *ApJ*, 524, 262

- Margutti R., 2009, PhD thesis, Univ. Bicocca, Milan, <http://boa.unimib.it/handle/10281/7465>
- Margutti R., Bernardini G., Barniol Duran R., Guidorzi C., Shen R. F., Chincarini G., 2011, MNRAS, 410, 1064
- Morsony B. J., Lazzati D., Begelman M. C., 2010, ApJ, 723, 267
- Narayan R., Kumar P., 2009, MNRAS, 394, L117
- Norris J. P., Nemiroff R. J., Scargle J. D., Kouveliotou C., Fishman G. J., Meegan C. A., Paciesas W. S., Bonnell J. T., 1994, ApJ, 424, 540
- Norris J. P., Nemiroff R. J., Bonnell J. T., Scargle J. D., Kouveliotou C., Paciesas W. S., Meegan C. A., Fishman G. J., 1996, ApJ, 459, 393
- Paciesas W. S. et al., 1999, ApJS, 122, 465
- Panaitescu A., Spada M., Mészáros P., 1999, ApJ, 522, L105
- Perna R., Armitage P. J., Zhang B., 2006, ApJ, 636, L29
- Proga D., Zhang B., 2006, MNRAS, 370, L61
- Rees M. J., Mészáros P., 1994, ApJ, 430, L93
- Rizzuto D. et al., 2007, MNRAS, 379, 619
- Ryde F., Borgonovo L., Larsson S., Lund N., von Kienin A., Lichti G., 2003, A&A, 411, L331
- Sakamoto T. et al., 2011, ApJS, 195, 2
- Scargle J. D., Norris J., Bonnell J., 1998, in Meegan C., Preece R., Koshut T., eds, AIP Conf. Proc. 428, Gamma-ray Bursts. Am. Inst. Phys., New York, p. 181
- Spada M., Panaitescu A., Mészáros P., 2000, ApJ, 537, 824
- Spergel D. N. et al., 2003, ApJS, 148, 175
- Temperton C., 1983, J. Comput. Phys., 52, 1
- van der Klis M., 1989, in Ögelman H., van den Heuvel E. P. J., eds, NATO/ASI Ser. C, Vol. 262, Timing Neutron Stars, Kluwer, Dordrecht, p. 27
- Vetere L., Massaro E., Costa E., Soffitta P., Ventura G., 2006, A&A, 447, 499
- Walker K. C., Schaefer B. E., Fenimore E. E., 2000, ApJ, 537, 264
- Zhang B., 2011, Comptes Rendus Phys., 12, 206
- Zhang B., Yan H., 2011, ApJ, 726, 90
- Zhang B., MacFadyen A., Wang P., 2009, ApJ, 692, L40

This paper has been typeset from a \LaTeX file prepared by the author.